# Dynamic boundary element - finite element analysis of railway bridges considering soil-structure-track interaction *

Paul König

*Universität Innsbruck, Unit of Applied Mechanics, Technikerstr. 13*
*Innsbruck, 6020, Austria*
*paul.koenig@uibk.ac.at*

Christoph Adam†

*Universität Innsbruck, Unit of Applied Mechanics, Technikerstr. 13*
*Innsbruck, 6020, Austria*
*christoph.adam@uibk.ac.at*

This paper investigates how soil-structure interaction affects the dynamic behavior of railway bridges. It uses a three-dimensional coupled finite element-boundary element modeling approach. This formulation applies to both the frequency and time domains, ensuring a consistent representation of wave propagation and radiation damping in the supporting soil. After outlining the underlying numerical framework, the focus is on the dynamic analysis of a single-span steel-girder railway bridge. The novel contribution of this study is in the comprehensive application of a three-dimensional coupled finite element-boundary element model of a steel railway bridge to assess the combined influence of soil and track modeling on both modal properties and transient response within a unified frequency-time domain numerical framework. The results demonstrate that soil-structure interaction and track can significantly affect the dynamic characteristics and response amplitudes of steel railway bridges. The findings underscore the importance of explicitly accounting for these effects when assessing the dynamic performance of railway bridges, particularly when evaluating serviceability limit states governed by vibration criteria.

*Keywords*: Bridge dynamics; Dynamic subsystem interaction; Boundary elements; Finite elements; Computational framework.

## 1. Introduction

Soon after the construction of the first high-speed railway lines in France, the destabilization of the ballast was observed on several bridges along the line. This phenomenon was attributed to excessive vibrations caused by resonance effects.[1] As a consequence, a maximum limit for the admissible bridge-deck acceleration of 3.5 $m/s^2$ for ballasted railway bridges was introduced in the EN1990-A1.[2] To ensure compliance with this limit, reliable response predictions must be performed during the design phase using numerical or analytical models. In engineering practice,

*Preprint of an article accepted for publication in *International Journal of Structural Stability and Dynamics* © 2026 World Scientific Publishing Company. `https://www.worldscientific.com/worldscinet/ijssd`
†Corresponding author

however, soil-structure interaction is often neglected and the track superstructure is frequently modeled in a simplified manner in order to limit computational effort.

Recent numerical investigations[3–10] accompanied by experimental validations[10,11] have demonstrated the significant influence of soil-structure interaction on the dynamic response of short-span railway bridges. In particular, portal-frame railway bridges have been investigated and it was shown that the effective modal damping ratios, accounting for soil-structure interaction, can largely exceed the admissible values prescribed in the EN1991-2[12] due to their embedding in the surrounding soil.[3,10,11] Similar trends of increased damping due to soil-structure interaction have been reported for reinforced and prestressed simply-supported concrete bridges.[4–7] These effects are especially relevant in resonance conditions induced by uniformly spaced axle loads moving at so-called *resonance speeds*, where damping has a decisive influence on the predicted structural response. Although soil-structure interaction effects have been extensively studied for portal-frame and concrete simply-supported railway bridges, numerical investigations focusing on steel bridges are limited. Nevertheless, studies in König et al.[8,9] reported similar effects, such as increased damping and shifted natural frequencies for steel bridges using simplified beam-based models that incorporate soil-structure interaction. Early[1] and recent[13] experimental investigations on steel bridges also showed significantly higher damping ratios than the recommended design values of the EN1991-2.[12] For steel bridges, representing the category with the lowest admissible damping ratios,[12] the spread of measured damping ratios is considerable, with values of up to 7 % reported.[13] Furthermore, the influence of the ballast stiffness and damping on steel bridges has been investigated experimentally[14] and numerically[15] using a simplified beam model. These studies indicate that the track substantially contributes to the overall system stiffness and damping.

Despite these findings, a clear gap remains in the numerical investigation of steel railway bridges using detailed, three-dimensional models that consistently account for soil-structure interaction and track-bridge interaction. Many existing studies rely on simplified *Euler-Bernoulli* beam formulations[5–9,16] combined with substructure approaches in which the soil is represented by spring-dashpot elements. While these models are well-suited for probabilistic analyses that account for uncertainties arising from the material properties of the soil,[17,18] they introduce significant simplifications. Thus, comparison with more detailed modeling strategies is needed. More sophisticated numerical approaches use finite elements to discretize parts of the soil volume,[11] or use boundary elements to discretize part of the soil surface.[4] These approaches enable the consideration of foundation-soil-foundation interaction effects that are neglected in simpler models. In the case of soil discretization using finite elements, the soil volume must be truncated, and artificial, non-reflective boundary conditions must be introduced to prevent elastic wave reflections. Such absorbing boundary conditions are commonly modeled using infinite elements,[19] or perfectly matched layers.[20] These requirements increase modeling complexity and computational cost. In contrast, boundary element formulations inherently account

for wave propagation towards infinity and therefore allow the soil surface to be discretized without the need for additional absorbing boundary conditions. This makes the method particularly well-suited for analyzing soil-foundation interaction problems.

This paper examines the impact of soil-structure interaction on the dynamic behavior of railway bridges via a comprehensive numerical study of a single-span steel-girder bridge. The adopted modeling approach combines finite element representations of the track-bridge-foundation system with a boundary element idealization of the supporting soil. This allows for a realistic description of wave propagation and radiation damping effects in the soil. This formulation can be used both in the frequency and time domains, allowing for the assessment of system dynamics based on the modal properties as well as under transient railway loading. Since the focus of this publication lies on the analysis of soil-structure interaction, complex train-bridge interaction[21] is neglected and the train is considered by a moving single load model according to EN1991-2.[12]

The coupled model is used to examine how variations in soil stiffness affect the global dynamic characteristics of the bridge-track system. Frequency-domain analyses are carried out to determine natural frequencies, effective modal damping ratios, and associated mode shapes. These analyses emphasize the contribution of the track and surrounding soil to the overall stiffness and energy dissipation of the system. Subsequently, time-domain simulations of train passages are performed to quantify the impact of soil-structure interaction on bridge accelerations and displacements. The results underscore the significance of considering soil-structure interaction effects when assessing the dynamic performance of railway bridges, particularly with regard to serviceability-related response measures.

## 2. Dynamic coupled boundary element - finite element implementation

For the present study of the effect of soil-structure interaction on the dynamic response of railway bridges subjected to high-speed trains, the computational software `MDdyn` (Multi-Domain-Dynamics) based on three-dimensional boundary element[22] and finite element formulations[23] has been developed. The frequency-domain formulation implemented in this software is used to identify the modal properties of the interacting system consisting of track, steel bridge, foundation, and soil. The time-domain formulation, also implemented, is employed to numerically predict the time-history response of the bridge due to high-speed traffic. The subsequent sections summarize the core aspects of the underlying numerical implementations.

### 2.1. *Boundary element domain*

Special attention is given to the implementation of boundary element procedures. Singular integrals inherent to the boundary element method are solved universally

for the frequency- and time-domain formulations. Additional element subdivision is performed for time-domain computations. The boundary element formulations assume homogeneous elastic material properties characterized by the *Young*'s modulus $E$, the *Poisson*'s ratio $\nu$, and the density $\rho$. The following sections outline these considerations as they apply to the present implementation.

### 2.1.1. *Frequency-domain formulation*

The time-harmonic solutions for the boundary displacements $u_k(\mathbf{x},\omega)$ and tractions $p_k(\mathbf{x},\omega)$ are derived from the boundary integral formulation in the frequency domain according to[22]

$$\begin{aligned} C_{lk}^{(i)}(\mathbf{x}^{(i)})u_k(\mathbf{x}^{(i)},\omega) = &\int_\Gamma \hat{u}_{lk}^*(\mathbf{r},\omega)p_k(\mathbf{x},\omega)\mathrm{d}\Gamma \\ &- \fint_\Gamma \hat{p}_{lk}^*(\mathbf{r},\omega)u_k(\mathbf{x},\omega)\mathrm{d}\Gamma \end{aligned} \tag{2.1}$$

where $C_{lk}^{(i)}$ represents the so-called *free term*, which depends on the surface geometry at the collocation point $\mathbf{x}^{(i)}$. The full-space singular fundamental solutions of the displacement $\hat{u}_{lk}^*$ and the tractions $\hat{p}_{lk}^*$[22] depend on the distance vector $\mathbf{r} = \mathbf{x} - \mathbf{x}^{(i)}$ between collocation point $\mathbf{x}^{(i)}$ and observation point $\mathbf{x}$ at the boundary surface at the discrete frequency $\omega$. Both surface integrals on the right hand side of Eq. (2.1) involve singular integrands for the case where the observation point approaches the collocation point ($\mathbf{x} \mapsto \mathbf{x}^{(i)}$) due to the singularities inherent in the fundamental solutions of displacements and tractions. The first integrand in Eq. (2.1) is limited to a *weak singularity* of $\mathrm{O}(1/r)$, while the second integrand includes a *strong singularity* of $\mathrm{O}(1/r^2)$ and the corresponding integral is formulated in the sense of a *Cauchy Principal Value* (CPV) integral, denoted by the horizontal dash of the integral symbol. Discretization of the surface geometry and numerical integration of the singular and CPV integrals, discussed further in section 2.1.4, yield the system of equations for the time-harmonic frequency-domain procedure,

$$\mathbf{H}\left(\omega\right)\mathbf{u}_\mathrm{B}\left(\omega\right) = \mathbf{G}\left(\omega\right)\mathbf{p}_\mathrm{B}\left(\omega\right) \tag{2.2}$$

with the frequency-dependent system matrices $\mathbf{H}$ and $\mathbf{G}$ and the vectors of displacements and tractions $\mathbf{u}_\mathrm{B}$ and $\mathbf{p}_\mathrm{B}$.

In the frequency-domain formulation, viscous damping can be explicitly considered. This is achieved by applying the correspondence principle, defining the complex *Lamé* constants $\overline{G} = G(1 + i2\zeta)$, where $\zeta$ is the viscous damping ratio, $G = \frac{E}{2(1+\nu)}$ is the elastic shear modulus of the soil, and $\overline{\lambda} = \lambda(1 + i2\zeta)$ with $\lambda = \frac{\nu E}{(1+\nu)(1-2\nu)}$.[22]

2.1.2. *Time-domain formulation*

The time-domain boundary integral equation with zero initial conditions and body forces reads as[22]

$$C_{lk}^{(i)}(\mathbf{x}^{(i)})u_k(\mathbf{x}^{(i)},t) = \int_0^{t^+}\int_\Gamma u_{lk}^*(\mathbf{r},t-\tau)p_k(\mathbf{x},\tau)\mathrm{d}\Gamma\mathrm{d}\tau - \int_0^{t^+}\fint_\Gamma p_{lk}^*(\mathbf{r},t-\tau)u_k(\mathbf{x},\tau)\mathrm{d}\Gamma\mathrm{d}\tau \tag{2.3}$$

and is based on the convolution of the full-space time-domain singular fundamental solutions of displacements $u_{lk}^*$ and tractions $p_{lk}^*$[24] and the boundary-surface tractions and displacements $p_k$ and $u_k$. Similar to the frequency-domain boundary integral formulation of Eq. (2.1), the fundamental solutions in the time domain used in Eq. (2.3) are singular in $\mathrm{O}(1/r)$ and $\mathrm{O}(1/r^2)$, and the second spatial integral of Eq. (2.3) is formulated as a CPV integral. The integrations in Eq. (2.3) are performed in two steps. First, the integration in time is performed analytically using piecewise linear interpolation functions for the displacements and piecewise constant interpolation functions for the tractions for the $n = 1, ..., N_\mathrm{t}$ time steps.[25] Numerical integration is then performed on the spacial integrals, considering the singular integration of section 2.1.4 and additional element subdivision to improve the integration of the wavefront between compression and shear waves. This yields the discretized transient boundary integral equation for the $n$-th step,[22]

$$\mathbf{H}^{nn}\mathbf{u}_\mathrm{B}^n = \mathbf{G}^{nn}\mathbf{p}_\mathrm{B}^n + \sum_{m=1}^{n-1}[\mathbf{G}^{nm}\mathbf{p}_\mathrm{B}^m - \mathbf{H}^{nm}\mathbf{u}_\mathrm{B}^m] \tag{2.4}$$

where the system matrices $\mathbf{G}^{nm}$ and $\mathbf{H}^{nm}$ result from the spatio-temporal integration along the $(n-m)$-th time interval.

2.1.3. *Free term evaluation*

The *free term* matrix $\mathbf{C}(\mathbf{x}^{(i)})$ at a collocation node $\mathbf{x}^{(i)}$ is identical for static, time-harmonic, and transient boundary element formulations and, for the transient case, is non-zero only for the time step $n = m$ when the full-space fundamental solutions derived from a *Dirac*-delta impulse are considered. Mantič[26] presents a generally applicable algorithm for computing the $\mathbf{C}$ matrix at a boundary node with an arbitrary number of tangent planes belonging to adjacent elements. In the present implementation, this algorithm evaluates the *free term* matrix. Because only a finite part of the soil half-space is modeled, the computation of the $\mathbf{C}$ matrix requires the assumption that the flat surfaces or straight edges extend beyond the edges of the truncated mesh edges, as described in detail by König (2024).[27] Using this approximation, no reflections of spurious waves at the truncated mesh edges were observed in the results of this paper or the separate verification examples reported in König (2024).[27]

### 2.1.4. *Singular integration*

Guiggiani and Gigante[28] show the numerical integration of the *strongly singular* CPV integral involving the elastostatic fundamental solution of tractions by performing element-wise integration of the elements containing the singular node $\mathbf{x}^{(i)}$. This procedure was originally developed for elastostatics, however, the similarities in the singularities of the time-harmonic fundamental solutions[22] and time-domain fundamental solutions[24] motivate adopting the procedure of Guiggiani and Gigante[28] for the frequency- and time-domain formulations of this paper. The validity of this approach is discussed briefly below.

To apply this method, the singular remainder inside the second integral of Eqs (2.1) and (2.3) must have the form,[28]

$$\overline{P}_{lk} = \frac{1}{r^2}\left[n_k(\mathbf{x})\frac{x_l - x_l^i}{r} - n_l(\mathbf{x})\frac{x_k - x_k^i}{r}\right] \tag{2.5}$$

For the frequency-domain formulation of Eq. (2.1), this condition is inherently satisfied, as shown by Guiggiani.[29] In the time-domain formulation of Eq. (2.3), the time integration is carried out before spatial integration. As demonstrated by König,[27] this yields an expression similar to that of Eq. (2.5). It reads as follows,

$$\overline{P}_{lk}^{nm} = \frac{1}{r^2}\left[D^{(\mathrm{I})}n_k(\mathbf{x})\frac{x_l - x_l^i}{r} + A^{(\mathrm{I})}n_l(\mathbf{x})\frac{x_k - x_k^i}{r}\right] \tag{2.6}$$

where $nm$ again denotes the discrete time difference in the convolution. The factors $D^{(\mathrm{I})}$ and $A^{(\mathrm{I})}$ result from analytic time integration. As shown by König,[27] these factors reduce to $A^{(\mathrm{I})} = -D^{(\mathrm{I})}$ and are independent of $\mathbf{r}$ for the piecewise linear interpolation of displacements. Therefore, they can be moved in front of the spatial integral, resulting in the same singular remainder as Eq. (2.5).

### 2.1.5. *Element subdivision for the transient formulation*

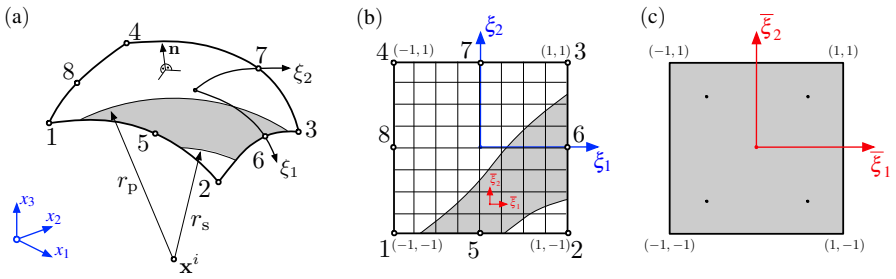



Fig. 1. Isoparametric 8-node element with highlighted integration region in (a) the global coordinate system, (b) the intrinsic coordinate system, with element subdivision ($\mathrm{N}^{\mathrm{sub}} = 8$), and (c) the subregion of integration with four *Gauss* points ($\mathrm{G}^{\mathrm{sub}} = 2$) (modified from Marrero and Domínguez[24])

In addition to the consideration of singular integrals, the transient time-domain boundary element formulation requires the integration of possible discontinuous integrals on an element at a given time step. This is due to the fact that there are only non-zero integral kernels between the two wave fronts of compression and shear waves (cf. Fig. 1(a), $r_\mathrm{p}$ and $r_\mathrm{s}$ at a given time step). To improve the numerical integration, the base element is further subdivided (cf. Fig. 1(b)). Integration is then performed sub-element by sub-element in the $\overline{\xi}_1$, $\overline{\xi}_2$ coordinate system of Fig. 1(c) using *Gaussian* integration, as for example done by Marrero and Domínguez.[24]

Since the integration of only a part of the element surface is also relevant for the singular case where the collocation node $\mathrm{x}^{(i)}$ is on the element, element subdivision is also performed here. This is done for each triangular integration domain resulting from the formulation of polar integration of the singular cases using $\rho\vartheta$-coordinates. Depending on the intrinsic coordinates $\boldsymbol{\eta}$, the three main cases depicted in Fig. 2 arise for quadrilateral elements with up to nine nodes. Each of the triangles (white and light blue) is subdivided into sub-regions of integration illustrated by the gray dashed lines, and the index $g$ corresponds to the $g$-th *Gauss* point.

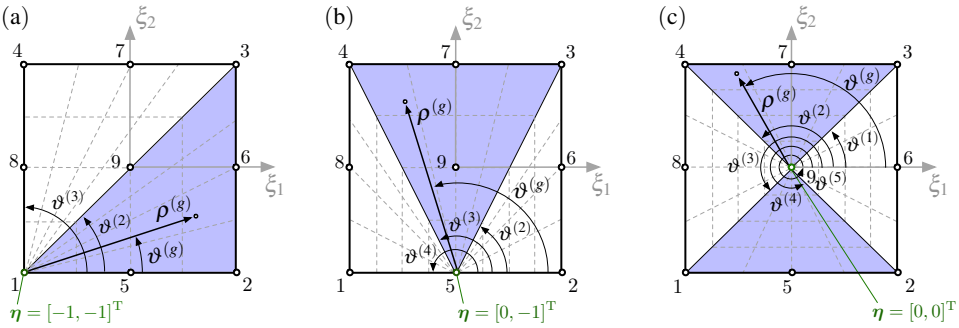



Fig. 2. Singular integration including element subdivision for the singular node at (a) a corner node, (b) an edge node, (c) the center node (modified from Guiggiani and Gigante[28]).

### 2.1.6. *Stability improvement*

The time-domain boundary element method is known to be prone to numerical instabilities.[30] In addition to element subdivision (cf. Figs 1 and 2), which improves numerical accuracy and stability, the stability improvement of Marrero and Domínguez[24] based on the linear combination of multiple time steps is applied in transient analyses.

### 2.1.7. *Verification of the boundary element implementation*

The results of an in-depth verification of the transient boundary element implementation are presented in König (2024).[27] This section summarizes relevant verification

results and supplemented them with an additional verification of the frequency-domain implementation. The verification example of the boundary element implementations in the time and frequency domains is the classic example of an infinite elastic layer subjected to a uniform surface traction,[22] as displayed in Fig. 3(a). A finite prism with the dimensions of $2\times2\times4$ meters is modeled from this infinite layer using quadratic 8-node quadrilateral boundary elements with an element length of $L_\mathrm{e} = 0.25$ m. The side and bottom surfaces are held fixed in the perpendicular direction, and normal unit traction is applied to the top surface in the vertical direction. For the transient computations, this surface traction is activated at the beginning of the computation and remains constant for the rest of the computation, i.e.,

$$p(t) = p_0 H(t) \tag{2.7}$$

where $H(t)$ denotes the *Heaviside* step function. For the time-harmonic frequency-domain computations, the traction is applied as

$$p(t) = p_0 e^{i\omega t} = \cos(\omega t) + i\sin(\omega t) \tag{2.8}$$

The elastic material properties are given by the *Young*'s modulus $E = 100$ MPa, the

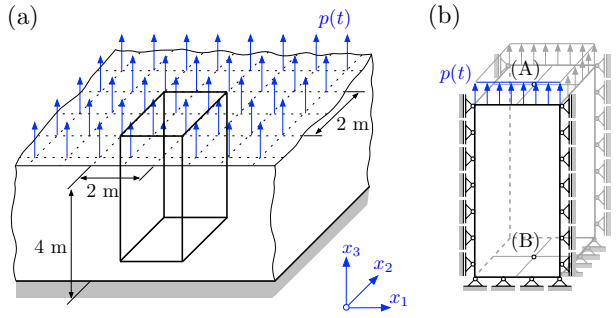



Fig. 3. Verification example of an infinite elastic layer. (a) Infinitely extending geometry and (b) finite section used in the analysis (modified from Marrero and Domínguez (2003)[24]).

*Poisson*'s ratio $\nu = 0.25$ and the density $\rho = 1000$ kg/m$^3$. The resulting compression wave velocity is $c_\mathrm{p} = 346.41$ m/s and the shear wave velocity is $c_\mathrm{s} = 200$ m/s.

For time-domain computations the time-step is selected based on the stability criterion[22]

$$\Delta t = \frac{L_\mathrm{e}}{c_\mathrm{p}}\beta_\mathrm{p} \tag{2.9}$$

Here, $\beta_\mathrm{p}$ denotes the stability parameter, which is typically chosen close to or above one to obtain stable results.[22]

The results of the time-domain computations are shown in Fig. 4. To assess the stability behavior of the implementation, the stability parameter was selected to have a low value of $\beta_\mathrm{p} = 0.5$. Figure 4 displays the results of the time-domain

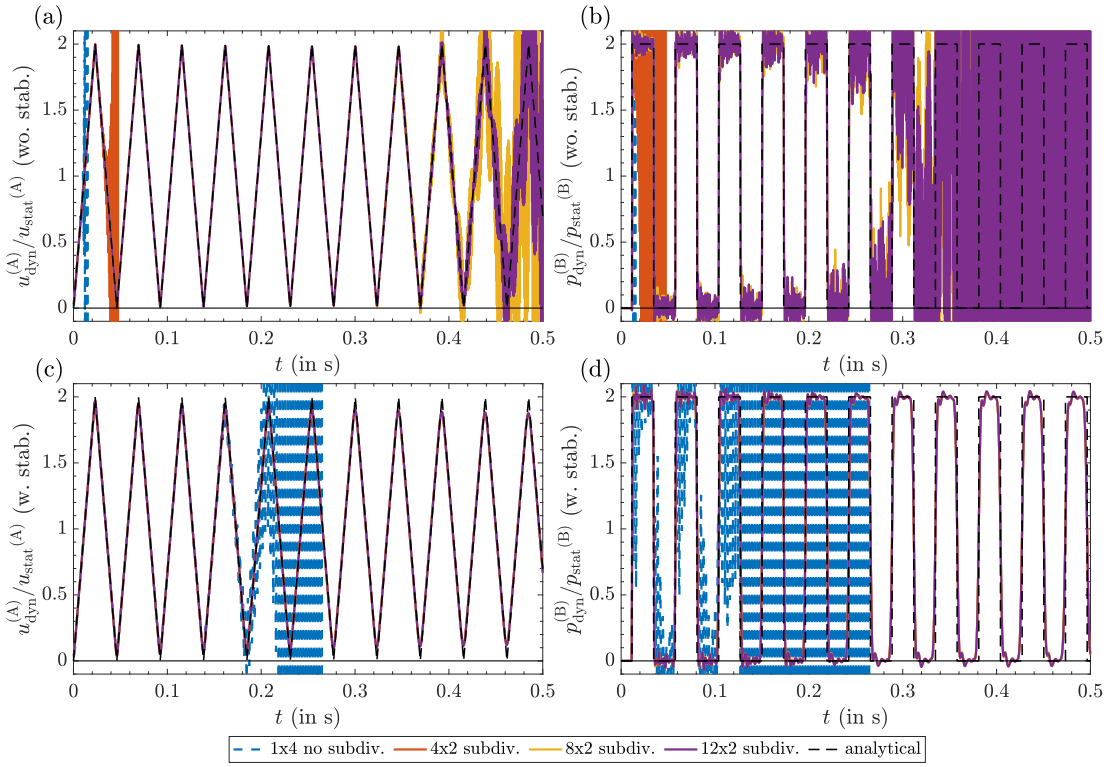



Fig. 4. Time histories with $\beta_p = 0.5$. First row: (a) Vertical displacement in (A) and (b) vertical tractions in (B) for computations without stability improvement. Second row: (c) Vertical displacement in (A) and (d) vertical tractions in (B) for computations with stability improvement of Marrero and Domínguez (2003)[24] (modified from König (2024)[27]).

computations due the step load of Eq. (2.7) at the center point of the top surface (A) and the center point of the bottom surface (B). The results of Figs 4 (a) and (b) were derived without applying the stability improvement ("wo. stab."), while the results of Figs (c) and (d)[24] where derived by applying the stability improvement ("w. stab.").[24] The dynamic displacement response at point (A), denoted as $u^{(A)}_{dyn}$, is normalized by the static solution easily derived from the solution of a 1D tension rod. It reads

$$u^{(A)}_{stat} = \frac{p_0 A L}{E_s A} \tag{2.10}$$

where the cross sectional area of the prism is $A = 2 \times 2$ m$^2$, the length is $L = 4$ m and the constrained modulus is $E_s = \frac{E(1-\nu)}{(1+\nu)(1-2\nu)} = 120$ MPa. Additionally, the dynamic traction results at point (B) were normalized by the static traction result

$$p^{(B)}_{stat} = -p_0 \tag{2.11}$$

For comparison, the normalized analytical dynamic reference solution of the 1D tension rod is also shown in Fig. 4 as a black dashed line.

A variety of different integration configurations were examined and denoted by $N^{\mathrm{sub}} \times G^{\mathrm{sub}}$, where $N^{\mathrm{sub}}$ corresponds to the number of element subdivisions per intrinsic coordinate and $G^{\mathrm{sub}}$ is the number of *Gauss* points per coordinate direction and subdivision. For a single quadrilateral element, the total number of *Gauss* points is given by $(N^{\mathrm{sub}})^2 \times (G^{\mathrm{sub}})^2$. The results of Figs 4 (a) and (b) show numerical instabilities for all configurations. However, a clear trend emerges with the refinement of the element integration. While the results with no element subdivision and four *Gauss* points per coordinate direction ("$1 \times 4$ no subdiv.") remain stable only for a very brief period, stability increases gradually with the number of subdivisions $N^{\mathrm{sub}}$ while keeping the number of *Gauss* points per subdivision and coordinate direction low ($G^{\mathrm{sub}} = 2$). There is only a slight improvement when refining from "$8 \times 2$ subdiv." to "$12 \times 2$ subdiv.". Figures 4 (c) and (d) show, that applying the stability improvement method of Marrero and Domínguez (2003)[24] further improves the stability of the results, leading to stable results for the computations using also element subdivision "subdiv.". The results agree very well with the analytical solution is very good, and the combined use of element subdivision and stability improvement is suitable for the application example in the later sections of this contribution. For additional studies involving different element types, element sizes, and stability parameters $\beta_{\mathrm{p}}$, see König (2024).[27]

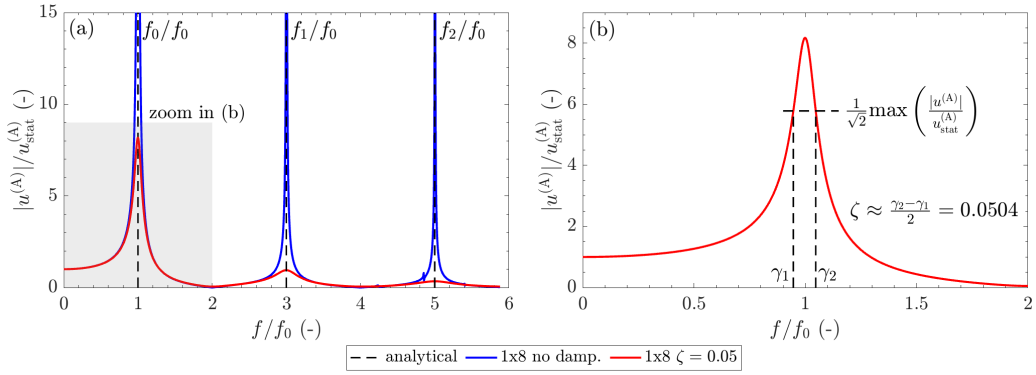



Fig. 5. Normalized frequency response displacement amplitude in point (A). (a) Comparison of response peaks with analytical resonance frequencies and (b) Verification of damping consideration using the half-power bandwidth method.[31]

Figure 5 (a) shows the vertical displacement amplitude $|u^{(\mathrm{A})}|$ at point (A) of the same problem geometry subjected to the harmonic loading according to Eq. (2.8) as a function of frequency. Here, the frequency is normalized by the fundamental resonance frequency of the elastic prism $f_0$. The analytical solutions of the $n = 1, 2, ..., \infty$ resonance frequencies of the system are given by

$$f_n = \frac{2n+1}{2}\frac{c_{\mathrm{p}}}{2L} \tag{2.12}$$

Comparing these resonance frequencies with the computed response peaks in Fig. 5 shows a very good agreement, further validating the time-harmonic frequency-domain implementation. The frequency-domain computations were performed with no element subdivision $N^{\text{sub}} = 1$ and $G^{\text{sub}} = 8$ *Gauss* points because further refinement of the integration does not significantly improve the results.[22] Since the frequency-domain formulation also permits the consideration of viscous damping, Fig. 5 (a) also shows the results of a computation assuming a damping of $\zeta = 5$ %, resulting in reduced resonance peaks. To verify the correct damping of the model, a zoom in into these results around the fundamental frequency is provided in Fig. 5 (b). The simple half-power bandwidth method[31] can be used to graphically verify the accurate application of the damping of $\zeta = 5$ %. The estimated damping ratio of $\zeta = 5.04$ % (see Fig. 5) agrees very well with the applied value of 5 %. The results of Fig. 5 are in good alignment with the analytical resonance frequencies, which concludes the verification of the boundary element implementations with accurate consideration of damping.

## 2.2. *Finite element domain*

With a focus on the boundary element procedures, the software `MDdyn` imports the geometry and system matrices of the finite element model of the structure and track from the commercial finite element software `ABAQUS`,[19] allowing for the use of a wide range of well-established finite element types.

### 2.2.1. *Frequency-domain formulation*

The time-harmonic finite element subsystem equations in the frequency domain read as follows[32]

$$(\mathbf{K} + i\omega\mathbf{C} - \omega^2\mathbf{M})\mathbf{u}_{\text{F}}(\omega) = \mathbf{f}_{\text{F}}(\omega) \tag{2.13}$$

or simply

$$\mathbf{D}(\omega)\mathbf{u}_{\text{F}}(\omega) = \mathbf{f}_{\text{F}}(\omega) \tag{2.14}$$

In Eq. (2.13), the matrices $\mathbf{M}$, $\mathbf{C}$, $\mathbf{K}$ represent the mass, damping and stiffness matrices of the linear finite element model. The vector $\mathbf{u}_{\text{F}}$ contains the vector of nodal displacements and rotations and $\mathbf{f}_{\text{F}}$ is the vector of nodal forces and moments.

### 2.2.2. *Time-domain formulation*

In general, the equations of motion of the discretized finite element domain read[23]

$$\mathbf{M}\ddot{\mathbf{u}}_{\text{F}}(t) + \mathbf{C}\dot{\mathbf{u}}_{\text{F}}(t) + \mathbf{K}\mathbf{u}_{\text{F}}(t) = \mathbf{f}_{\text{F}}(t) \tag{2.15}$$

with the mass, damping, and stiffness matrices $\mathbf{M}_{\text{F}}$, $\mathbf{C}_{\text{F}}$, $\mathbf{K}_{\text{F}}$, the vector of nodal forces and moments $\mathbf{f}_{\text{F}}$, and the vector of nodal displacements and rotations $\mathbf{u}_{\text{F}}$. Equation (2.15) can be written as[23]

$$\mathbf{D}\mathbf{u}_{\text{F}}^{n} = \mathbf{f}_{\text{eff}}^{n} \tag{2.16}$$

after application of the *Newmark-β* algorithm[23] in the $n$-th time step. Here, $\mathbf{D}$ represents the effective dynamic stiffness matrix and $\mathbf{f}_{\text{eff}}^{n}$ is the effective load vector of the $n$-th step.

### 2.3. *Boundary element - finite element coupling procedures*

The coupling procedures in the frequency and time domains consider conforming meshes of the interface between the finite element domain and the boundary element domain. Therefore, compatibility – i.e., equality of nodal displacements of the coinciding boundary element and finite element nodes at the common interface (subscript "c") – is prescribed by

$$\mathbf{u}_{\text{Bc}} = \mathbf{u}_{\text{Fc}} \tag{2.17}$$

Furthermore, the equality of forces must be satisfied, requiring that the nodal forces evaluated at the coinciding nodes must be of equal magnitude and in opposite direction,

$$\mathbf{f}_{\text{Bc}} = -\mathbf{f}_{\text{Fc}} \tag{2.18}$$

Taking these conditions into account, a *direct coupling* procedure is used to condense the degrees of freedom of boundary elements and finite elements into a global system of equations for the coupling of the equations in the frequency domain, i.e., Eqs (2.2) and (2.14).[33,34]

For the coupling of the time-domain formulations, a *direct* approach that enforces compatibility and equilibrium at each time step could also be used.[30,34] This, however, requires the same time step for the finite element and boundary element domains, a condition that is not needed in more complex *iterative coupling* approaches. Since it is often advantageous to use different time steps for the boundary element and finite element domains, such an *iterative coupling* procedure in the form of the algorithm of von Estorff and Hagen[35] is used for the coupling of the equations in the time domain (Eqs (2.4) and (2.16)). The detailed formulation of the iterative coupling of the time-domain formulations can be found in von Estorff and Hagen (2006).[35] However, applying this coupling procedure requires the definition of suitable parameters, consisting of the four convergence tolerances $\varepsilon_{\text{u}}$, $\varepsilon_{\text{f}}$, $\varepsilon_{\text{v}}$, $\varepsilon_{\text{g}}$, relaxation parameters $\omega_{\text{u}}$ and $\omega_{\text{f}}$, and the interpolation parameter $\vartheta$.[35] Several computations were conducted using this iterative scheme. The parameters were chosen according to Table 1. As outlined in the convergence study of von

Table 1. Tolerances and parameters applied for the iterative coupling according to.[35]

| $\varepsilon_{\text{u}} = \varepsilon_{\text{v}}$ | $\varepsilon_{\text{f}} = \varepsilon_{\text{g}}$ | $\omega_{\text{u}}$ | $\omega_{\text{f}}$ | $\vartheta$ | $\Delta t_{\text{FE}}/\Delta t_{\text{BE}}$ |
|---|---|---|---|---|---|
| $10^{-4}$ | $10^{-6}$ | 0.8 | 0.8 | 0.2 | 0.25 |

Estorff and Hagen (2006),[35] the combination of $\omega_{\text{u}} = \omega_{\text{f}} = 0.8$ and $\vartheta = 0.2$ leads

to a good convergence behavior for the time step ratio of $\Delta t_{\mathrm{FE}}/\Delta t_{\mathrm{BE}} = 0.25$ used for the application examples. The convergence tolerances $\varepsilon_{\mathrm{u}}$, $\varepsilon_{\mathrm{f}}$, $\varepsilon_{\mathrm{v}}$, and $\varepsilon_{\mathrm{g}}$ are all chosen one magnitude smaller than the values suggested values of von Estorff and Hagen (2006).[35] Therefore, they are significantly stricter than the suggested values and lead to a good accuracy in the subsequent analyses of the application examples.

König (2024)[27] analyzed additional application examples considering soil-structure interaction involving the coupled boundary element - finite element implementation. Comparisons were also made between the numerical solutions and the analytical model of Wolf and Deeks (2004).[36]

## 3. Modal properties of the steel-girder bridge

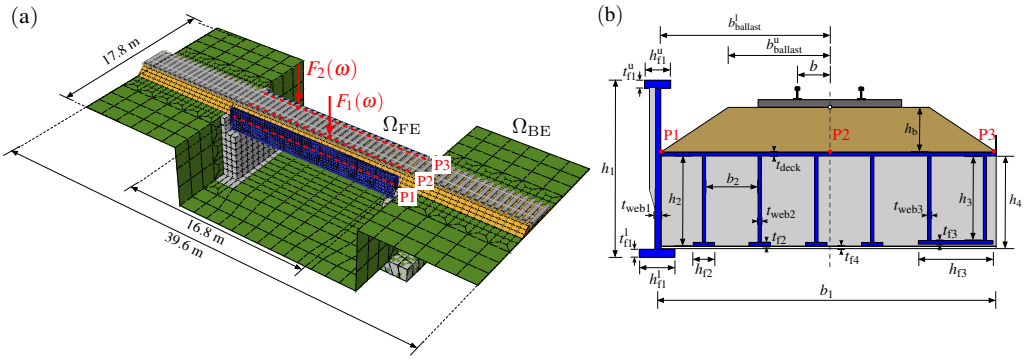



Fig. 6. Geometry of the investigated steel-girder bridge. (a) Numerical model of the structure discretized by finite elements ($\Omega_{\mathrm{FE}}$) with the boundary element model of the soil ($\Omega_{\mathrm{BE}}$). (b) Cross-section of the steel-girder bridge (modified from Salcher and Adam (2015)[37]).

In the following, the presented software is used to investigate the influence of track-structure and soil-structure interaction on the modal properties of a bridge structure, since its dynamic response excited by high-speed traffic depends to a large extent on these properties. In particular, a single-span steel-girder bridge with a span length of 16.8 m is considered. Figure 6(a) shows the complete system of track and bridge discretized with finite elements ($\Omega_{\mathrm{FE}}$), coupled with the soil, discretized with boundary elements ($\Omega_{\mathrm{BE}}$). The total width of the boundary element mesh is 17.8 m and its length is 39.6 m. The track extends an additional 11.4 m before and after the steel girder bridge. This distance is large enough to ensure that the artificially introduced boundary conditions at each end of the track do not influence the bridge response.[38] The geometry of the cross-section illustrated in Fig. 6(b) is taken from Salcher and Adam (2015).[37] For further reference, the dimensions are listed in Table 8 of the appendix.

The bearing at the foundation located on the left in Fig. 6(a) is realized as pinned, coupling all displacements of the steel bridge with the bearing seat of the

foundation. Relative displacements of the steel bridge and the bearing seat in Fig. 6 are possible only in the longitudinal direction of the bridge. Since the vertical displacements between the bridge structure and the foundation are coupled at the bearing, this model accounts for stiff bearings, such as steel bearings, and does not consider bearings with lower stiffness, such as elastomeric bearings. The material parameters of the ballast are taken from literature[11,39] and listed together with the ballast dimensions in Table 9. Further parameters of the track are specified in Table 11. The dimensions and discretization of the concrete foundation are shown in Fig. 7 and the corresponding material parameters are listed in Table 10.

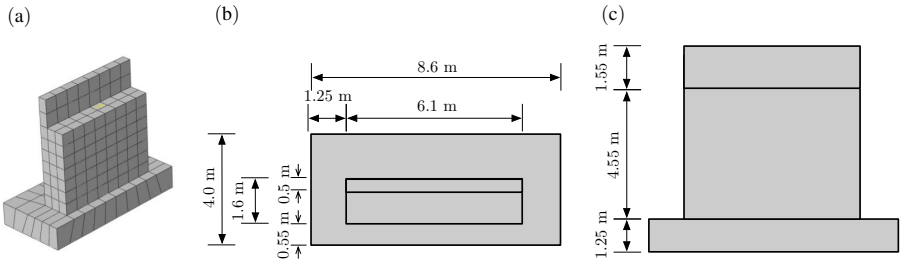



Fig. 7. Foundation of the bridge structure. (a) Meshed geometry. (b) Top view. (c) Front view.

Quadratic 20-node finite continuum elements (C3D20) are used for the discretization of the ballast, the foundation and the sleepers. The structure of the bridge is modeled with 3- and 4-node linear shell elements (S3 and S4) and 3-node quadratic beam elements (B32) are used for the rails. Using this discretization, the finite element domain $\Omega_{\mathrm{FE}}$ has a total of $N_{\mathrm{FE}} = 94,077$ active degrees of freedom. The boundary element domain $\Omega_{\mathrm{BE}}$ of the soil, discretized with 8-node quadratic quadrilateral boundary elements, has a total of $N_{\mathrm{BE}} = 10,077$ degrees of freedom with soil material parameters listed in Table 2.

First, soil–structure interaction is neglected in section 3.2, and the foundation and soil are therefore assumed to be rigid. Only the domain $\Omega_{\mathrm{FE}}$ with fixed boundary conditions at the interface nodes is considered. Two variations of the structural model are considered herein. In "Model 1", only the mass of the track, which is uniformly distributed on the deck plate of the steel-girder bridge, is taken into account. "Model 2" includes an FE model of the full track subsystem (see "Model 1" and "Model 2" in Fig. 8).

Subsequently, the model is expanded in section 3.3 to include the soil, which is discretized using the proposed boundary element formulation. Again, two model variants are considered: in "Model 3" (Fig. 8), only the track mass added uniformly to the deck plate is included, whereas "Model 4" contains the complete track model (see Fig. 6(a) and "Model 4" in Fig. 8). Here, the *Young*'s modulus of the soil $E_{\mathrm{so}}$ is varied from 25 to 700 MPa ($\Delta E_{\mathrm{so}} = 25$ MPa) for soils of very low to high stiffness. The corresponding shear and compression wave velocities of the soil, $c_{\mathrm{s}}$

and $c_{\mathrm{p}}$, are listed in Table 3. This elastic range represents soils that vary from very loose/soft sand or clay ($c_{\mathrm{s}} \lesssim 150$ m/s), to loose sand or medium-stiff clay ($150 \lesssim c_{\mathrm{s}} \lesssim 210$ m/s), to medium-dense sand or stiff clay ($210 \lesssim c_{\mathrm{o}} \lesssim 300$ m/s), to dense sand or very stiff clay ($300 \lesssim c_{\mathrm{s}} \lesssim 374$ m/s).[40] The assumed *Poisson*'s ratio of $\nu = 0.25$ represents unsaturated or partially saturated soils. Saturated soils, where $\nu$ approaches values of 0.5, are not considered in the present study. In practice, soils with $E_{\mathrm{so}} \lesssim 100$ MPa (or $c_{\mathrm{s}} \lesssim 150$ m/s) typically require pile foundations. However, this numerical study of spread footings also includes such low-stiffness soils to understand their effect on structural dynamics.

Table 2. Soil parameters.

| Quantity | Variable | Unit | Value |
|---|---|---|---|
| Density | $\rho_{\mathrm{so}}$ | kg/m$^3$ | 2000 |
| *Poisson*'s ratio | $\nu_{\mathrm{so}}$ | - | 0.25 |
| *Young*'s modulus | $E_{\mathrm{so}}$ | MPa | $25 \div 700$ |

Table 3. Upper and lower bounds of the shear and compression wave velocity corresponding to the soil parameters in Table 2.

| Quantity | Variable | Unit | Value |
|---|---|---|---|
| Shear wave velocity | $c_{\mathrm{s}}$ | m/s | $70.7 \div 374.2$ |
| Compression wave velocity | $c_{\mathrm{p}}$ | m/s | $122.5 \div 648.1$ |

### 3.1. *Mesh verification*

The mesh size of the finite elements of the steel-girder bridge components matches the one used by Salcher and Adam (2015),[37] while the boundary element mesh resembles the size used by Romero, et. al (2013)[4] (cf. Fig. 6(a)). To assess the suitability of this discretization, a comparison is made with a refined mesh of the same geometry, where the average element length is half that of the analysis model of Fig. 6(a). The refined mesh geometry is shown in Fig. 9. This model has a total of $N_{\mathrm{FE}} = 303,210$ active finite element degrees of freedom and a total of $N_{\mathrm{BE}} = 40,887$ boundary element degrees of freedom. Verification is based on frequency-domain computations. According to Table 2, soil parameters are assumed to have a fixed value of $E_{\mathrm{so}} = 400$ MPa. Individual computations are performed with a harmonic force applied either at the center point of path P2 on the deck plate of the bridge (see $F_1(\omega)$ in Figs 6(a) and 9) or at the quarter point of path P3 (see $F_1(\omega)$ in Figs 6(a) and 9) at varying frequencies ranging from 0 to 45 Hz. For these two load cases, the vertical displacement response $w_{\mathrm{b3}}(\omega)$, at the second quarter point of path P3 (NR3 in Fig 9) is computed, and the corresponding frequency response

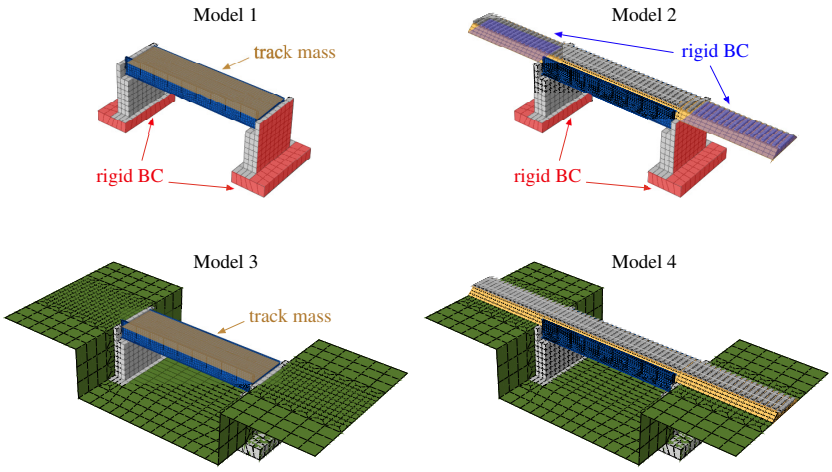



Fig. 8. Model 1: Structural model with track mass added to the deck plate and fixed boundary conditions at the foundations. Model 2: Structural model including the full track subsystem, with fixed boundary conditions at the foundations and at the base of the ballast before and after the bridge. Model 3: Soil-structure model with track mass added to the deck plate. Model 4: Soil-structure model including the full track subsystem.

functions (FRFs) are derived from

$$H_{3j}(\omega) = \frac{w_{\mathrm{b}3}(\omega)}{F_j(\omega)} \ , \quad j = 1, 2 \tag{3.1}$$

Since the model is linear, the FRFs are independent of the amplitude of the applied force and it can be chosen freely. For the present analysis, an amplitude of 10 kN was assumed for both $F_1(\omega)$ and $F_2(\omega)$.

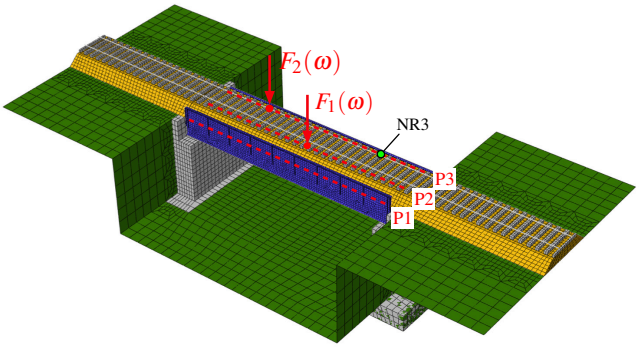



Fig. 9. Geometry of the coupled structure discredized by the refined "mesh 2", subjected to the concentrated harmonic force ($F_1(\omega)$, or $F_2(\omega)$), with response point NR3.

The absolute values of these FRFs are displayed in Fig. 10 and are compared for the the coarser "mesh 1" and the refined "mesh 2". As can be seen, the applying the force $F_1(\omega)$ to the center of the bridge deck mainly results in an excitation close to 11 Hz. On the other hand, applying force $F_2(\omega)$ to the quarter point of the edge of the bridge deck (path P3) yields an FRF with multiple distinct peaks within the considered frequency range of 0 to 45 Hz. These additional peaks correspond to the higher modes of the coupled system. Overall, the FRFs evaluated for "mesh 1" and "mesh 2" agree very well, showing that no significant improvement in results is achieved with further mesh refinement. Due to the substantially smaller computational effort required for the model discretized using "mesh 1", this mesh is used for all subsequent analyses.

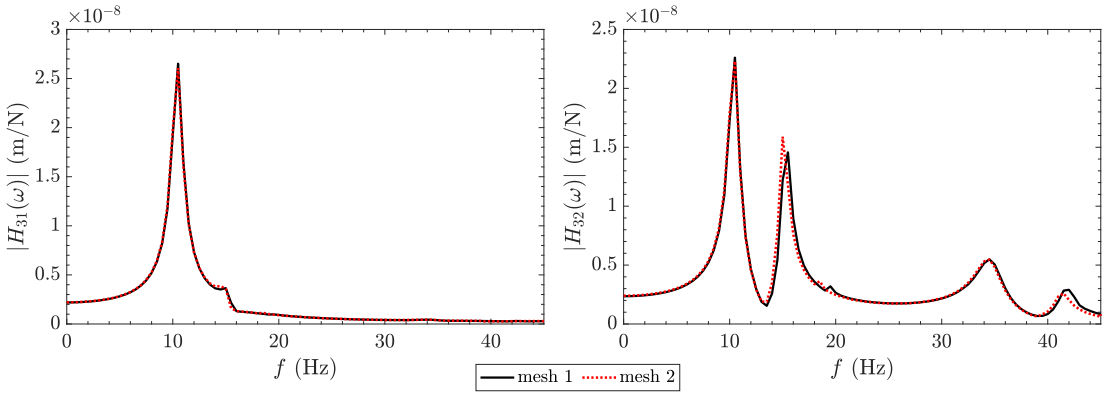



Fig. 10. Comparison of frequency response functions computed for the model discretized with "mesh 1" and "mesh 2".

### 3.2. *Models without soil-structure interaction*

The structural model neglecting soil-structure interaction is analyzed in two phases. Firstly, the stand-alone finite element model of the steel-girder bridge on a rigid foundation and rigid soil is considered, where the mass of the track components is simply added uniformly to the deck plate of the bridge ("Model 1" in Fig. 8). After determining the relevant modal parameters of this system, the full structural model of the coupled track-bridge system on rigid foundation is analyzed ("Model 2" in Fig. 8). Structural damping of the bridge, track and foundation is considered with *Rayleigh* damping, where the element damping matrix $\mathbf{C}^{(e)}$ is assumed to be proportional to the element mass matrix $\mathbf{M}^{(e)}$ and the element stiffness matrix $\mathbf{K}^{(e)}$,[41]

$$\mathbf{C}^{(e)} = \alpha_\mathrm{c}\mathbf{M}^{(e)} + \beta_\mathrm{c}\mathbf{K}^{(e)} \tag{3.2}$$

Alternatively, it can be expressed in terms of the $k$-th modal damping ratio,[41]

$$\zeta_k^{(\mathrm{R})} = \frac{\alpha_\mathrm{c}}{4\pi f_k} + \pi\beta_\mathrm{c} f_k \tag{3.3}$$

The *Rayleigh* coefficients $\alpha_\mathrm{c}$ and $\beta_\mathrm{c}$ are chosen based on a damping ratio of 0.5% for steel and a damping ratio of 2.0% for concrete and ballast components at two specific frequencies $f_1$ and $f_2$.

For this example problem, $f_1 = 9.96$ Hz, corresponding to the fundamental frequency of the rigidly supported bridge including the mass of the track (see Fig. 11(a)), and $f_2 = 100$ Hz, characterizing the maximum frequency of interest, are substituted into Eq. (3.3) to determine $\alpha_\mathrm{c}$ and $\beta_\mathrm{c}$. The corresponding coefficients are listed in Table 4.

Table 4. *Rayleigh* damping parameters for the structural components of the FE domain.

| Material | $\zeta_1^{(\mathrm{R})} = \zeta_2^{(\mathrm{R})}$ | $\alpha_\mathrm{c}$ | $\beta_\mathrm{c}$ |
|---|---|---|---|
| Steel | 0.5% | 0.5592 | $1.45 \cdot 10^{-5}$ |
| Concrete, ballast | 2.0% | 2.2765 | $5.7896 \cdot 10^{-5}$ |

Natural frequencies and effective damping ratios of the system can be derived from the homogeneous form of Eq. (2.15), rearranged in state space,[42]

$$\mathbf{A}\dot{\mathbf{z}}_\mathrm{h}(t) + \mathbf{B}\mathbf{z}_\mathrm{h}(t) = \mathbf{0} \tag{3.4}$$

where

$$\mathbf{A} = \begin{bmatrix} \mathbf{C} & \mathbf{M} \\ \mathbf{M} & \mathbf{0} \end{bmatrix}, \quad \mathbf{B} = \begin{bmatrix} \mathbf{K} & \mathbf{0} \\ \mathbf{0} & -\mathbf{M} \end{bmatrix}, \quad \mathbf{z}_\mathrm{h}(t) = \begin{bmatrix} \mathbf{u}_\mathrm{F} \\ \dot{\mathbf{u}}_\mathrm{F} \end{bmatrix} \tag{3.5}$$

Taking $\mathbf{z}_\mathrm{h}(t) = \boldsymbol{\phi}_k e^{s_k t}$ for the homogeneous solution, the eigenvalue problem[42]

$$(s_k\mathbf{A} + \mathbf{B})\,\boldsymbol{\phi}_k = \mathbf{0} \tag{3.6}$$

is obtained, which yields the eigenvalues in the form of complex conjugate pairs, often referred to as poles,[42]

$$s_k = -\zeta_k\omega_k + i\omega_k\sqrt{1-\zeta_k^2} \tag{3.7}$$

and the corresponding complex mode shapes $\boldsymbol{\phi}_k$, where $k = 1, ..., N_\mathrm{FE}$. The natural frequencies $f_k$ and the effective damping ratios $\zeta_k$ follow from Eq. (3.7),[42]

$$f_k = \frac{|s_k|}{2\pi}, \quad \zeta_k = -\frac{\Re(s_k)}{|s_k|} \tag{3.8}$$

### 3.2.1. *Model 1: structural model with track mass*

For the bridge on rigid supports and added track mass ("Model 1" in Fig. 8), the real parts of the first bending-dominated, first torsion-dominated, and second bending-dominated mode shapes $\Re(\boldsymbol{\phi}_k)$ are depicted in Fig. 11 along with the corresponding

natural frequencies and effective modal damping ratios. Since the stand-alone bridge is composed of steel components only, the modal damping ratios follow directly from the *Rayleigh* parameters for steel elements (Table 4) and Eq. (3.3) evaluated at the natural frequency of the corresponding mode. A clear asymmetry in the mode shape displacements can be observed in Fig. 11. This is explained by the higher stiffness of the cross-section at path P1 compared to path P3 illustrated in Fig. 6.

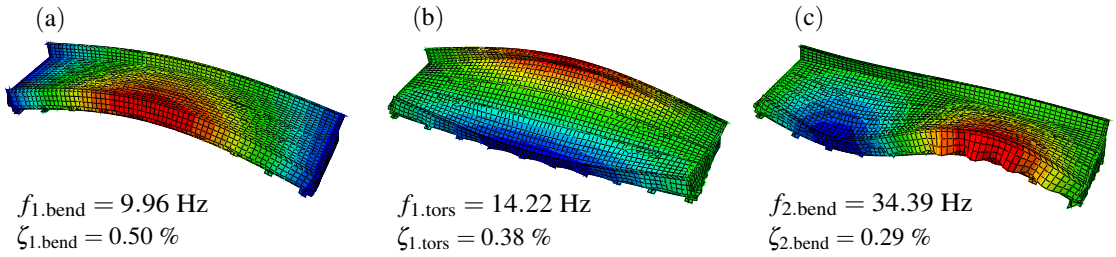



Fig. 11. Rigidly supported bridge structure with track mass. Real part of the mode shape, natural frequency, and effective damping ratio. (a) First bending-dominated mode, (b) first torsion-dominated mode, and (c) second bending-dominated mode.

### 3.2.2. *Model 2: structural model with full track*

Figure 12 shows the real parts of the mode shapes of the structural model considering the full track ("Model 2" in Fig. 8) with their corresponding natural frequencies and effective damping ratios. A clear influence of the increased system stiffness due to the full track subsystem can be seen in the natural frequencies of Fig. 12. The relative deviations in natural frequencies of the model with track mass only from the structural model with full track are listed in Table 5. The influence of the ballast stiffness on the natural frequencies of the coupled structure of bridge and track can be seen for all three modes considered and is very pronounced for the first bending- and torsion-dominated modes.

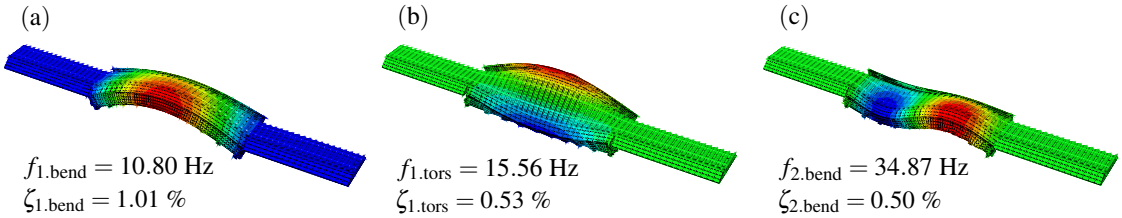



Fig. 12. Rigidly supported bridge structure with full track. Real part of the mode shapes, natural frequencies, and effective damping ratios. (a) First bending-dominated mode, (b) first torsion-dominated mode, and (c) second bending-dominated mode.

Table 5. Relative difference between the natural frequencies and the effective damping ratios $\Delta\zeta$ of the reduced structural model with track mass (Fig. 11) and those of the structural model with full track (Fig. 12).

| Natural frequency | Difference (in %) | Effective damping ratio | Difference (in %) |
|---|---|---|---|
| $\Delta f_{1.\text{bend}}$ | 7.78 | $\Delta\zeta_{1.\text{bend}}$ | 50.5 |
| $\Delta f_{1.\text{tors}}$ | 8.61 | $\Delta\zeta_{1.\text{tors}}$ | 28.3 |
| $\Delta f_{2.\text{bend}}$ | 1.38 | $\Delta\zeta_{2.\text{bend}}$ | 42.0 |

Table 6. Effective modal damping ratios of the first bending–
dominated, first torsion-dominated and second bending-dominated modes depending on the damping ratio applied for the ballast material ($\zeta_1^{(\text{R,bal})} = \zeta_2^{(\text{R,bal})}$).

| $\zeta_1^{(\text{R,bal})} = \zeta_2^{(\text{R,bal})}$ | $\zeta_{1.\text{bend}}$ | $\zeta_{1.\text{tors}}$ | $\zeta_{2.\text{bend}}$ |
|---|---|---|---|
| 1 % | 0.70 % | 0.42 % | 0.38 % |
| 2 % | 1.01 % | 0.53 % | 0.50 % |
| 3 % | 1.35 % | 0.64 % | 0.64 % |

Due to the higher damping of the ballast compared to the damping of the steel components, the effective modal damping ratios of the model with track are significantly larger. The effective damping ratios of the bridge model, where the track is considered by its mass only, deviate from those of model including the full track by up to 50.5 % for the first bending-dominated mode, as shown in Table 5. As shown by the experimental investigations of Stollwitzer et al. (2023)[14] and the numerical study of König and Adam (2024),[15] this increase in damping and stiffness is related to track-bridge interaction mechanisms in the longitudinal direction. On the other hand, vertical track-bridge interaction only influences the load-distributing effect of the track and only affects the response of short-span bridges.[43] Correspondingly, a change in rail pad stiffness in the longitudinal direction leads to a change in the overall stiffness and natural frequencies. Assuming a longitudinal rail pad stiffness value of $k_{\text{rx}} = 49$ MN/m (see Table 11) results in the natural frequencies listed in Fig. 12. Taking a smaller value of $k_{\text{rx}} = 24.5$ MN/m results in $f_{1.\text{bend}} = 10.64$ Hz, $f_{1.\text{tors}} = 15.55$ Hz, and $f_{2.\text{bend}} = 34.76$ Hz, and assuming a larger value of $k_{\text{rx}} = 73.5$ MN/m yields slightly higher natural frequencies $f_{1.\text{bend}} = 10.88$ Hz, $f_{1.\text{tors}} = 15.57$ Hz, and $f_{2.\text{bend}} = 34.94$ Hz. However, changing $k_{\text{rx}}$ only has a negligible effect on the modal damping ratios.

To more clearly see the influence of ballast damping on the modal damping ratio of the structural model with the full track, the modal damping ratio applied to the ballast material in the form of *Rayleigh* damping $\zeta_1^{(\text{R,bal})} = \zeta_2^{(\text{R,bal})}$ has been varied in Table 6. The corresponding effective modal damping ratios of the first bending-dominated, first torsion-dominated and second bending-dominated modes are listed in Table 6. A clear increase of the overall damping is observed as the ballast damping increases. This trend has also been observed by Stollwitzer et al. (2023)[14] and König and Adam (2024).[15]

### 3.3. *Models with soil-structure interaction*

Considering the significant influence of the track on the overall system stiffness and damping in case of the rigid soil, the soil-structure interaction model is at first analyzed with the track mass only ("Model 3" in Fig. 8) and then with the full track (Fig. 6(a) and "Model 4" in Fig. 8). For the coupled soil-structure system, where the soil surface is discretized by boundary elements, the eigenvalue problem becomes non-linear due to the frequency-dependent boundary element system matrices (c.f. Eq. (2.2)). Therefore, the eigenvalues are not computed directly but an indirect approach based on frequency-domain evaluations is performed. To this end, a harmonic concentrated force is applied to the bridge deck in the vertical direction and the resulting displacements are computed. Depending on the mode shapes to be estimated, the analyses are performed with the force $F_1(\omega)$ or the force $F_2(\omega)$ with different application points as shown in Fig. 6. The corresponding FRFs are then computed for all displacement degrees of freedom of the model, from which the modal properties are estimated. Since the soil-structure interaction system has closely spaced and highly damped modes, the accuracy of the identified modal parameters depends highly on the estimation method used. The subsequent analyses use the least-squares complex frequency-domain (LSCF[44]) method. Its effectiveness in identifying highly damped, closely spaced modes has been documented in Van der Auweraer et. al (2001)[44] and Peeters et. al (2004).[45] To reliably identify the stable physical poles, a model-order range $[N_{\min}, N_{\max}]$ is defined, where $N_{\min}$ and $N_{\max}$ are the minimum and maximum orders, respectively. The LSCF algorithm is applied to each model order within this range, and the identified natural frequencies and damping ratios (see Eq. (3.8)) are stored. Then, the assessment of stability is carried out for each identified mode based on the stability criteria

$$\frac{|f_k^{(N_{\max})} - f_k^{(n)}|}{f_k^{(N_{\max})}} \leq 0.01 \tag{3.9}$$

$$\frac{|\zeta_k^{(N_{\max})} - \zeta_k^{(n)}|}{\zeta_k^{(N_{\max})}} \leq 0.05 \tag{3.10}$$

where $k$ denotes the $k$-th mode and $n = N_{\min}, N_{\min}+1, ..., N_{\max}-1$ the model order. A pole is considered as stable only if the criteria of Eqs (3.9) and (3.10) are met for at least 20% of the model order range considered.

#### 3.3.1. *Model 3: soil-structure model with track mass*

In this section, the influence of soil-structure interaction on the modal parameters of the coupled bridge-foundation-soil system is analyzed. As before, the mass of the track is simply added to the deck plate of the steel-girder bridge ("Model 3" in Fig. 8). Considering the soil density and the *Poisson*'s ratio from Table 2, the modal parameters are first analyzed for a fixed soil *Young*'s modulus of $E_{\text{so}} = 200$

MPa. Taking into account all active degrees of freedom and the time-harmonic force $F_1(\omega)$ applied to the center of the bridge structure, the corresponding real parts of the first 18 complex-valued mode shapes $\Re(\boldsymbol{\phi}_k)$ are estimated and plotted in Fig. 13. For each mode, the natural frequency $f$ and damping ratio $\zeta$ are shown in Fig. 13. The identified mode shapes can be classified into three main categories, which are *primary structural modes*, where bending and torsion modes of the steel-girder structure dominate the mode shape (Fig. 13(1a)–(1c)), *non-structural modes*, which are mainly governed by deformations of the surrounding soil (Fig. 13(2a)–(2j)), and *secondary structural modes* involving only locally isolated deformations of the steel members (Fig. 13(3a)–(3e)).

To separate these categories of modes, which are differently affected by soil-structure interaction, the modal collinearity factor (MCF) or modal phase collinearity (MPC) is commonly used, e.g. by Zangeneh et al.[46] Pappa et al.[47] define the MPC based on the variances and covariances of the real and imaginary parts of the complex modes given by $S_{xx} = \Re(\boldsymbol{\phi}_k)^{\mathrm{T}}\Re(\boldsymbol{\phi}_k)$, $S_{yy} = \Im(\boldsymbol{\phi}_k)^{\mathrm{T}}\Im(\boldsymbol{\phi}_k)$, and $S_{xy} = \Re(\boldsymbol{\phi}_k)^{\mathrm{T}}\Im(\boldsymbol{\phi}_k)$ reading as

$$\mathrm{MPC}(\boldsymbol{\phi}_k) = \frac{(S_{xx} - S_{yy})^2 + 4S_{xy}^2}{(S_{xx} + S_{yy})^2} \tag{3.11}$$

The terms MCF and MPC are often used interchangeably, with MCF defined as[48]

$$\mathrm{MCF}(\boldsymbol{\phi}_k) = 1 - \mathrm{MPC}(\boldsymbol{\phi}_k) \tag{3.12}$$

The MPC quantifies the correlation of phase angles at the degrees of freedom for a given mode. It ranges from 0 for completely uncorrelated phase angles to 1 for completely correlated phase angles, and thus also quantifies the complexity of the mode shape, with a maximum value of 1 for real-valued modes. Since the non-classical damping associated with the wave propagation in the soil is the main contributor to the complexity of the mode shapes, lower MPC values indicate modes with a proportionally larger contribution of the soil to the overall system deformation.

The secondary structural modes are least affected by the soil, as indicated by MPC values larger than 0.9 and the relatively low damping ratio below 3 %, as seen in Fig. 13(3a)–(3e). The primary structural modes, such as the first bending-dominated mode (1a), the first torsion-dominated mode (1b), and second bending-dominated mode (1c), have moderate to high MPC values (0.45 to 0.90) and damping ratios ranging from 1.4 % for the first torsion-dominated mode to 10.7 % for the first bending-dominated mode. The non-structural modes (2a)–(2j) have higher damping ratios ranging from 8.8 % to 70.0 %. In addition, their corresponding MPC values tend to be closer to 0, with the exception of modes (2c) and (2d) with MPC = 0.72 and MPC = 0.45, respectively. Both modes exhibit rigid-body-like displacements of the steel-girder bridge and deformations concentrated at the foundation and its surrounding soil, thus showing a considerable amount of damping (20.8 % and 25.3 % in Figs 13(2c) and (2d)). Similar modes resembling rigid-body

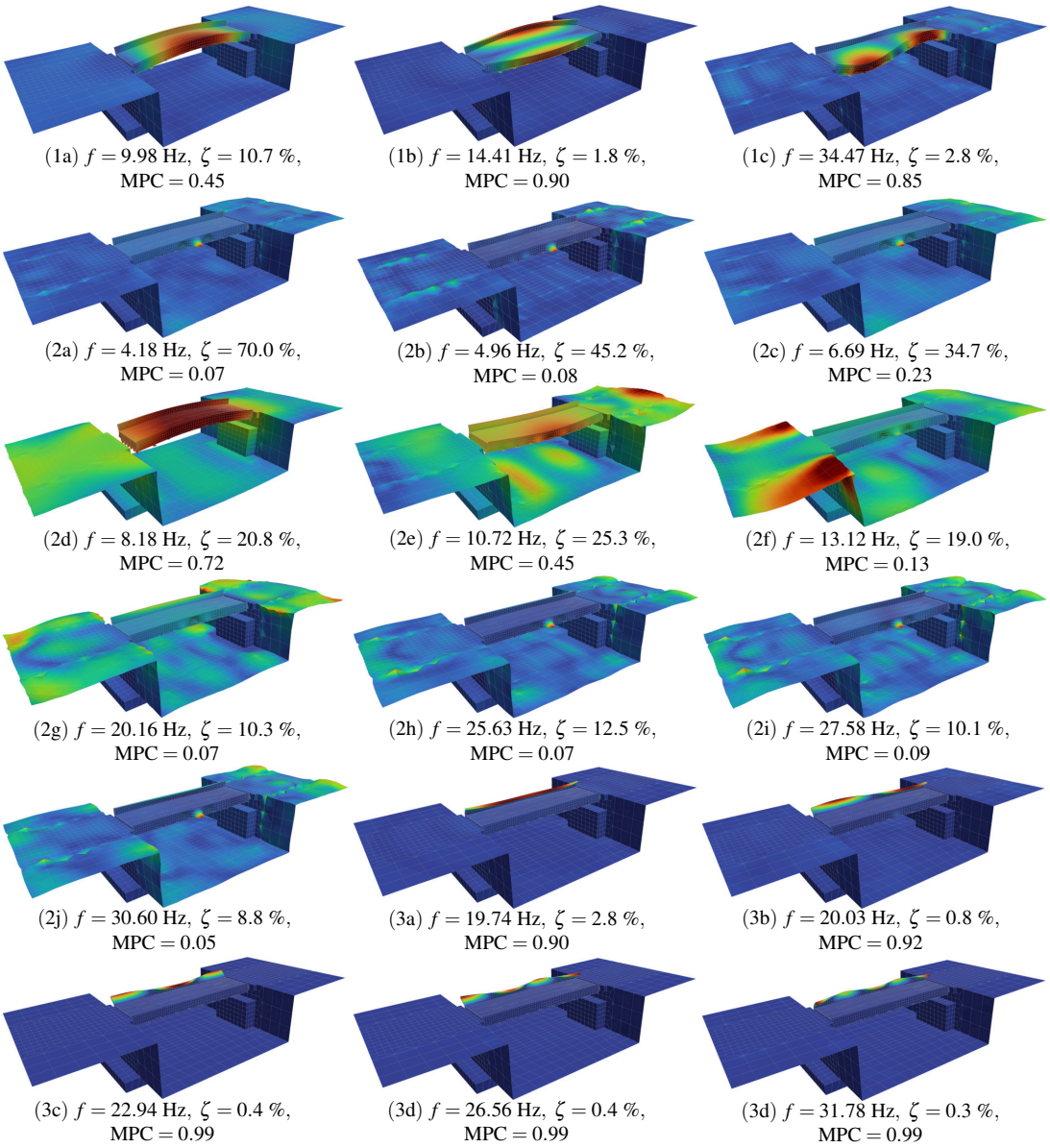



Fig. 13. Modal properties of the soil-structure interaction model with track mass and a soil *Young*'s modulus of $E_{\mathrm{so}} = 200$ MPa. Real parts of the first 18 mode shapes $\Re(\boldsymbol{\phi}_k)$ with their corresponding natural frequencies $f$, damping ratios $\zeta$, and modal phase collinearity (MPC). (1a)–(1c) Primary structural modes. (2a)–(2j) Non-structural modes. (3a)–(3e) Secondary structural modes.

modes also have been observed in reduced analytical beam models involving soil-structure interaction with damping ratios $> 60$ %.[8,27] Of the modes described

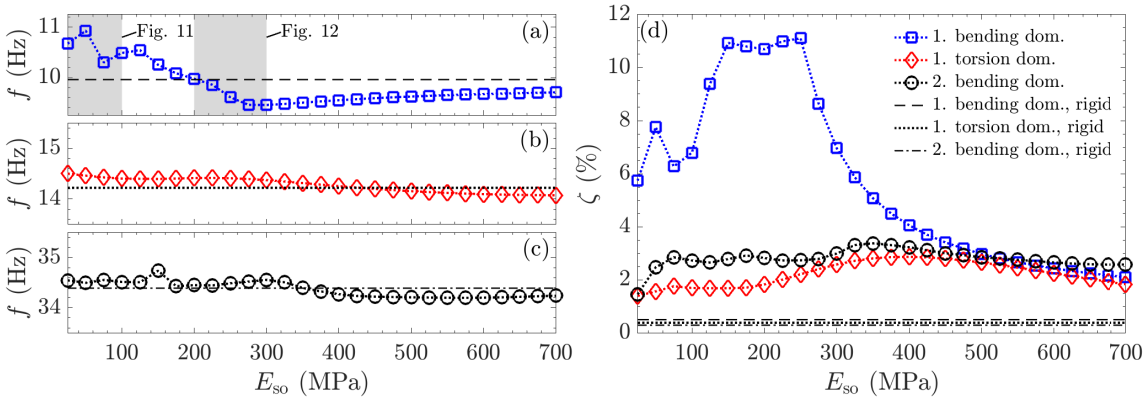



Fig. 14. Primary structural modes of the soil-structure interaction model with track mass as a function of soil modulus $E_{so}$. Natural frequency of (a) first bending-dominated mode, (b) first torsion-dominated mode, and (c) second bending-dominated mode. (d) Corresponding effective damping ratios.

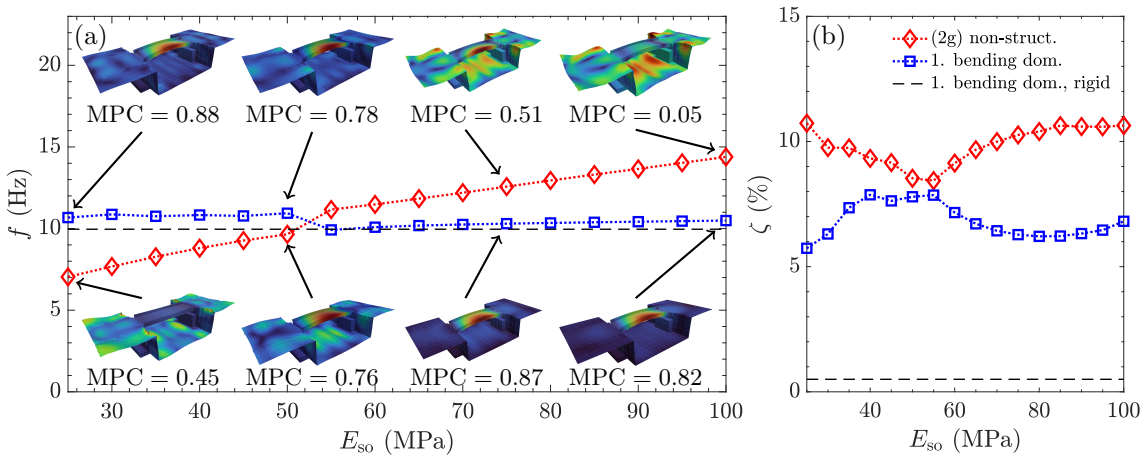



Fig. 15. First bending-dominated mode and closely-spaced non-structural mode for the soil *Young*'s modulus between $E_{so}$ = 25 MPa and $E_{so}$ = 100 MPa. (a) Natural frequencies and (b) effective damping ratios.

above, the primary structural modes of Figs 13(1a)–(1c) represent the counterparts to the modes of the rigidly supported structure depicted in Fig. 11.

Next, the dependence of natural frequencies and damping ratios on *Young*'s modulus of the soil is investigated. For this purpose, the *Young*'s modulus is varied within the range specified in Table 2. Since the influence of the soil on the secondary structural modes is small and the overall contribution of these modes to the bridge deck displacements and accelerations is considered as negligible, they are not analyzed further.

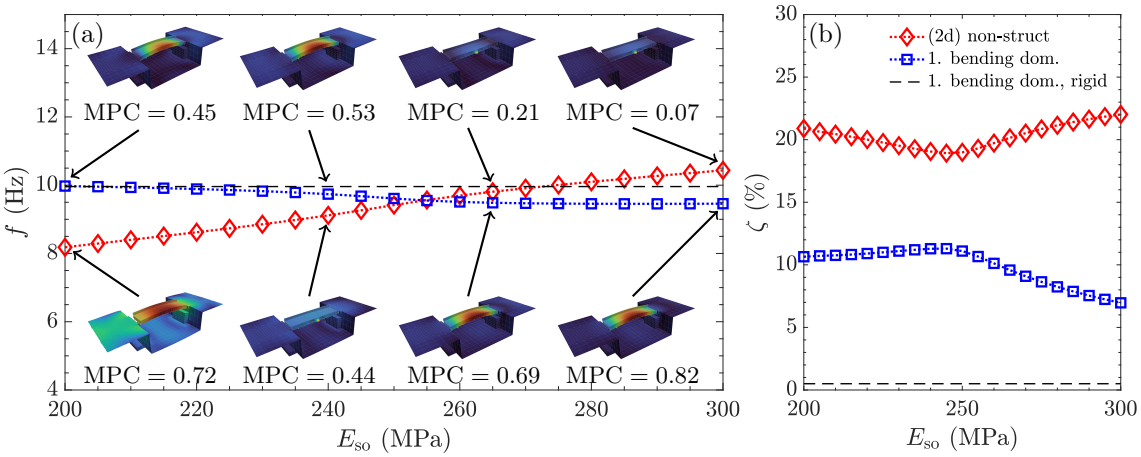



Fig. 16. First bending-dominated mode and closely-spaced non-structural mode for the soil *Young*'s modulus between $E_{so}$ = 200 MPa and $E_{so}$ = 300 MPa. (a) Natural frequencies and (b) effective damping ratios.

In contrast to the secondary structural modes, the primary structural modes are expected to dominate the response of the bridge deck excited by the passage of a train. Figure 14 depicts the natural frequencies of (a) the first bending-dominated mode, (b) the first torsion-dominated mode, and (c) the second bending-dominated mode for the considered range of soil *Young*'s moduli. In order to ensure sufficient excitation of the first bending-dominated and second bending modes for a reliable modal parameter estimation over the whole range of soil stiffness, the force $F_2(\omega)$ located at the quarter point of the path P3 is applied for the estimation of these two modes. Here, the largest influence of the soil *Young*'s modulus is visible for the natural frequency of the first bending-dominated mode (Fig. 14(a)). This strong dependence of the modal parameters of the first bending-dominated mode on the *Young*'s modulus is also visible in the corresponding effective modal damping ratio (Fig. 14(d)), which ranges from 2.10 % for the stiffest soil ($E_{so}$ = 700 MPa) to 11.10 % for soil of moderate stiffness ($E_{so}$ = 250 MPa). The modes with higher natural frequencies (b) and (c) are less influenced by the soil-structure interaction and have modal damping ratios below 4 % over the considered soil stiffness range. Overall, the natural frequencies of the bending- and torsion-dominated modes of the coupled bridge-soil system are close to those of the rigidly supported bridge, as shown by the dashed, dotted, and dash-dotted lines. However, the corresponding effective damping ratios are significantly higher for the coupled bridge-soil system than for the rigidly-supported bridge due to the additional geometrical damping of the soil.

Since a high variability of the natural frequency of the first bending-dominated mode, which is a primary mode, is observed for lower *Young*'s moduli, this mode is further analyzed in Figs 15 and 16. Figure 15(a) shows the natural frequency

of the identified first bending-dominated mode for *Young*'s moduli from $E_{\mathrm{so}} = 25$ MPa to $E_{\mathrm{so}} = 100$ MPa. In addition, the natural frequency of the closest non-structural mode corresponding to the one in Fig. 13(2g) is depicted in Fig. 15(a). The corresponding mode shapes are shown for four different *Young*'s moduli of the soil. While the separation of the two modes into a non-structural mode with a high contribution from the soil and the first primary structural bending-dominated mode is straightforward for $E_{\mathrm{so}} = 25$ MPa, $E_{\mathrm{so}} = 75$ MPa, and $E_{\mathrm{so}} = 100$ MPa, it is not easy for the case of $E_{\mathrm{so}} = 50$ MPa where the natural frequencies are closest to each other. For this case, the corresponding mode shapes show both a significant bending of the bridge and a moderate contribution from the soil. Also, the corresponding MPC values of 0.78 and 0.76 and damping ratios of 8.53 % and 7.80 % suggest that two similar bending-dominated modes can be identified for this particular soil stiffness. As the *Young*'s modulus of the soil increases, the separation of these two modes becomes more pronounced and is supported by the MPC value approaching 0 in the case of the non-structural mode and 1 in the case of the primary structural bending-dominated mode. It should be noted that the soft soil conditions ($E_{\mathrm{so}} \lesssim 100$ MPa) assumed in Fig. 15 would likely necessitate a piled foundation. Nevertheless, the results in Fig. 15 are valuable because they clearly show the evolution of closely spaced non-structural and primary structural modes for this bridge.

Figure 16 shows another case for a non-structural mode closely spaced to the first primary structural bending-dominated mode for the range $E_{\mathrm{so}} = 200$ MPa to $E_{\mathrm{so}} = 300$ MPa. Here, the natural frequency of the first rigid-body-like non-structural mode, also shown in Fig. 13(2d) for $E_{\mathrm{so}} = 200$ MPa, increases with $E_{\mathrm{so}}$. The visual distinction between the first primary structural bending-dominated mode and the non-structural rigid-body-like mode is simple here, and the separation of modal damping ratios is pronounced, as demonstrated in Fig. 16(b). However, comparing MPC values for low *Young*'s moduli in the range of this figure fails to identify the two types of modes, as for $E_{\mathrm{so}} = 200$ MPa, the non-structural rigid-body-like mode has an MPC value of 0.72, which is significantly larger than for the bending-dominated mode, which has a value of MPC = 0.45.

In addition, the natural frequencies and effective damping ratios of the first five non-structural modes (cf. Fig. 13(2a)–(2e)) are depicted in Fig. 17. A large influence of the soil *Young*'s modulus on the natural frequency of these modes can be observed in Fig. 17, as it increases continuously with increasing $E_{\mathrm{so}}$. The damping ratios associated with these modes tend to be higher and less dependent on the *Young*'s modulus of the soil. These observations align with the definition of non-structural modes, which are primarily governed by deformations of the surroundings. For these modes, a high dependence of the natural frequency on the soil stiffness is expected, given the significant contribution of soil deformations to the corresponding mode shapes. Since the main damping contribution results from geometrical damping inside the soil, these modes are also expected to have larger overall damping values. Primary structural modes, on the other hand, show mainly structural deformations, yielding lower overall damping ratios due to geometrical damping of the soil and

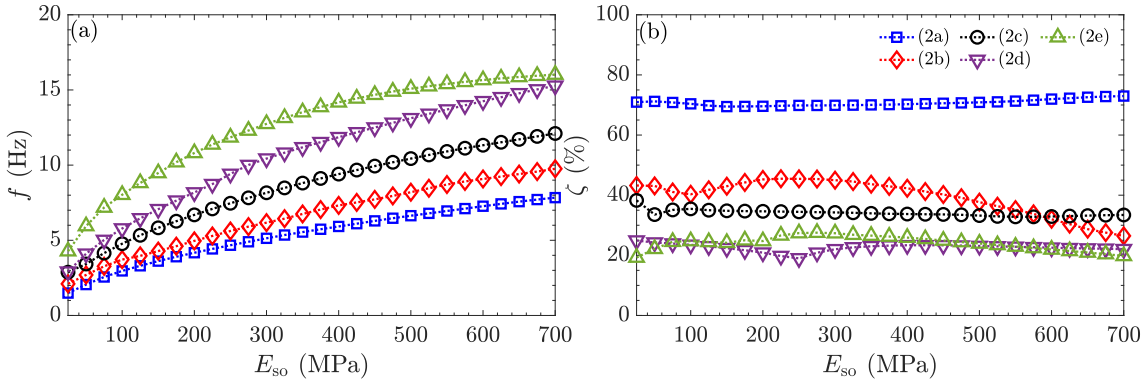



Fig. 17. Non-structural modes of the soil-structure model with track mass as a function of soil modulus $E_{\mathrm{so}}$. (a) Natural frequencies and (b) effective damping ratios.

a smaller dependence of the corresponding natural frequencies on the soil stiffness. These differences in the dependence of the natural frequencies on the soil stiffness directly lead to the observation that these two types of modes can have very closely spaced natural frequencies for certain *Young*'s moduli, as outlined in Figs 15 and 16.

### 3.3.2. *Model 4: soil-structure model with full track*

The complete interaction system of Fig. 6(a) ("Model 1" in Fig. 8), consisting of the track, the bridge, the foundation, and the soil, is analyzed in the same manner as the reduced model with added track mass of section 3.3.1. The mode shapes are determined for a *Young*'s modulus of the soil of $E_{\mathrm{so}} = 200$ MPa and the other soil parameters listed in Table 2, based on the frequency-domain computations applying the single force $F_1(\omega)$. Figure 18 shows the real parts of the first 18 mode shapes. As can be observed, the bending and torsion-dominated primary structural modes (see Fig. 18(1a)–(1c)) have the highest MPC values. The identified non-structural modes are shown in Figs 18(2a) to (2h). Similar to the model with added track mass, two rigid-body-like modes are identified in Fig. 18(2c) and (2e). They are associated with larger deformations of the soil and high effective modal damping ratios of 26.6 % and 18.6 %. The secondary structural modes are shown in Figs 18(3a) to (3e). Due to the importance of the primary structural bending-dominated and torsion-dominated modes for the response of the bridge deck, Fig. 19 shows their corresponding natural frequencies and effective modal damping ratios as a function of the soil *Young*'s modulus.

In addition, the influence of material damping of the soil can be considered in the present frequency-domain analysis. In a further analysis, material damping is assigned to the soil via a viscous damping ratio of $\zeta_{\mathrm{so}} = 2$ %. The corresponding results are shown in Fig. 19 with orange markers. As can be seen, the influence of this additional damping mechanism on the natural frequencies and damping ratios of the

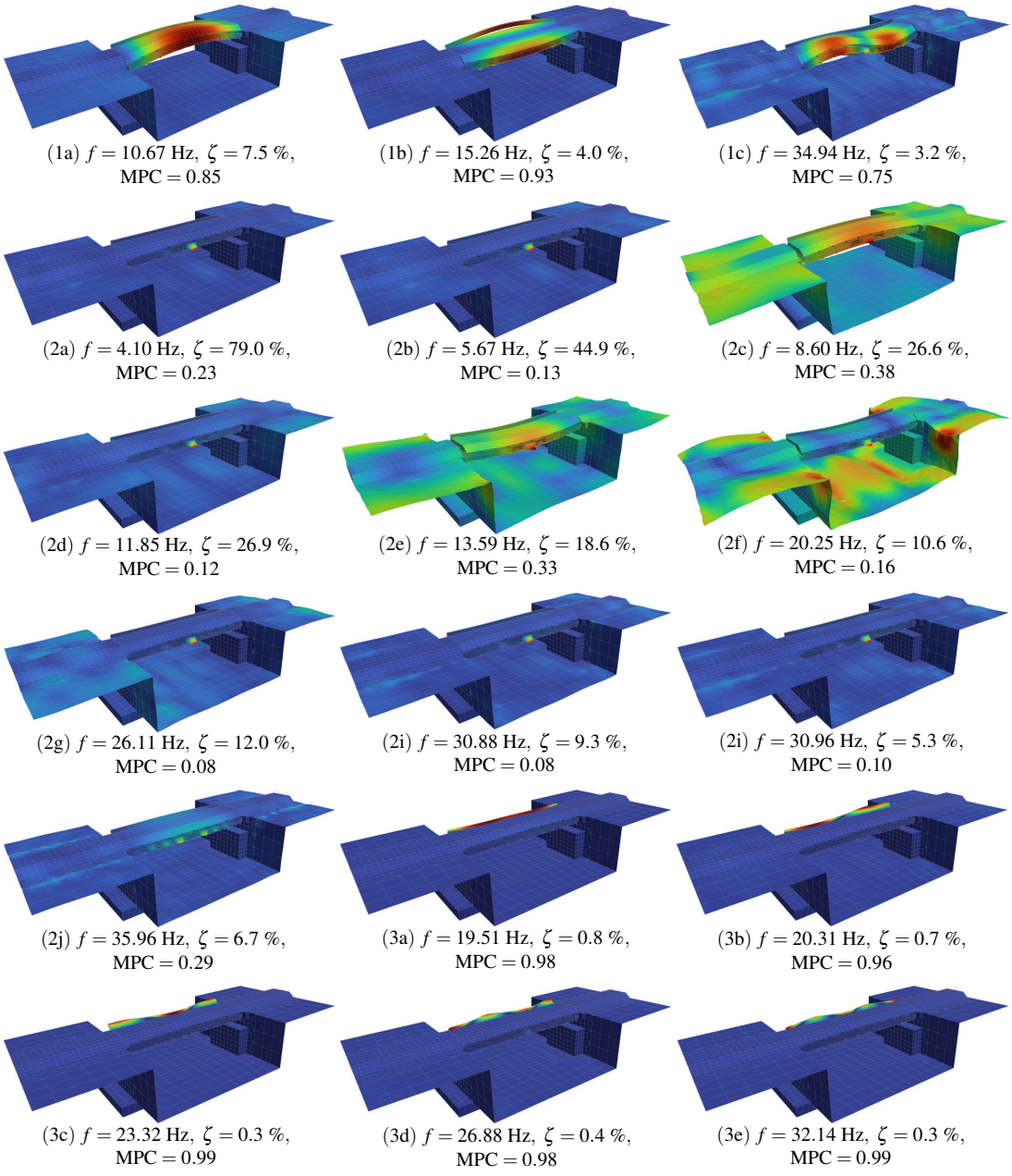



Fig. 18. Modal properties of the soil-structure model with full track and a soil *Young*'s modulus of $E_{\mathrm{so}} = 200$ MPa. Real parts of the first 18 mode shapes $\Re(\boldsymbol{\phi}_k)$ with their corresponding natural frequencies $f$, damping ratios $\zeta$, and modal phase collinearity (MPC). (1a)–(1c) Primary structural modes. (2a)–(2j) Non-structural modes. (3a)–(3e) Secondary structural modes.

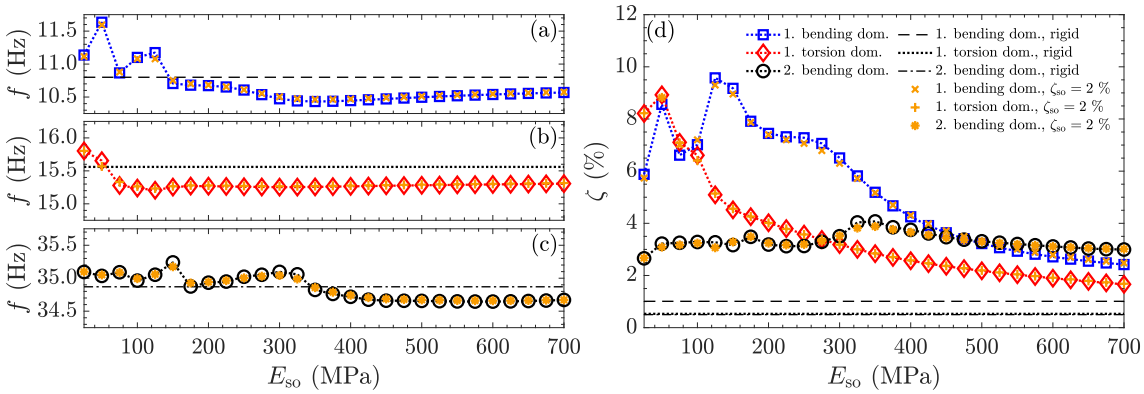



Fig. 19. Modal properties of the boundary element - finite element model with full track as a function of soil modulus $E_{so}$. Natural frequency of (a) first bending-dominated mode, (b) first torsion-dominated mode, and (c) red second bending-dominated mode. (d) Corresponding effective damping ratios.

primary structural bending- and torsion-dominated modes is negligible. Therefore, material damping of the soil is omitted in the subsequent analyses.

According to the EN1991-2,[12] the design damping ratio for the given steel-girder bridge with $L_b = 16.8$ m is 0.9 %. Thus, the estimated modal damping ratio for the first bending-dominated mode is 2.7 times the one of the recommended design value for the stiffest considered soil with $E_{so} = 700$ MPa and up to 10.6 times for the soil of lower stiffness ($E_{so} = 125$ MPa).

Overall, the influence of the track on the modal parameters of the bending-dominated and torsion-dominated structural modes is significant. This fact is visualized in Fig. 20, where the corresponding natural frequencies and damping ratios of the model with full track (results of Fig. 19) are compared with those of the model with added track mass (results of Fig. 11). As can be seen in Figs 20(a), (b), and (c), the increase in overall stiffness due to the track results in an increase in the natural frequencies of all three primary structural modes and for all soil stiffnesses.

Furthermore, for the first bending- and torsion-dominated modes, a strong dependence of the effective modal damping ratio on the soil *Young*'s modulus, together with the full track, is visible in Figs 20(d) and (e). While for low to medium stiff soil ($E_{so} = 125$ to $E_{so} = 300$ MPa), the estimated modal damping ratio of the model with track mass overestimates the modal damping ratio of the first bending-dominated mode by up to 53 %, the modal damping ratio for the stiffest soil is underestimated by up to 13 %. The opposite trend is observed for the first torsion mode, where for the soils of lower stiffness ($E_{so} < 350$ MPa) the modal damping ratio is underestimated for the model with added track mass, and the modal damping ratios are slightly overestimated for the higher stiffnesses ($E_{so} >= 350$ MPa). These discrepancies in the estimated modal damping ratios as a function of the

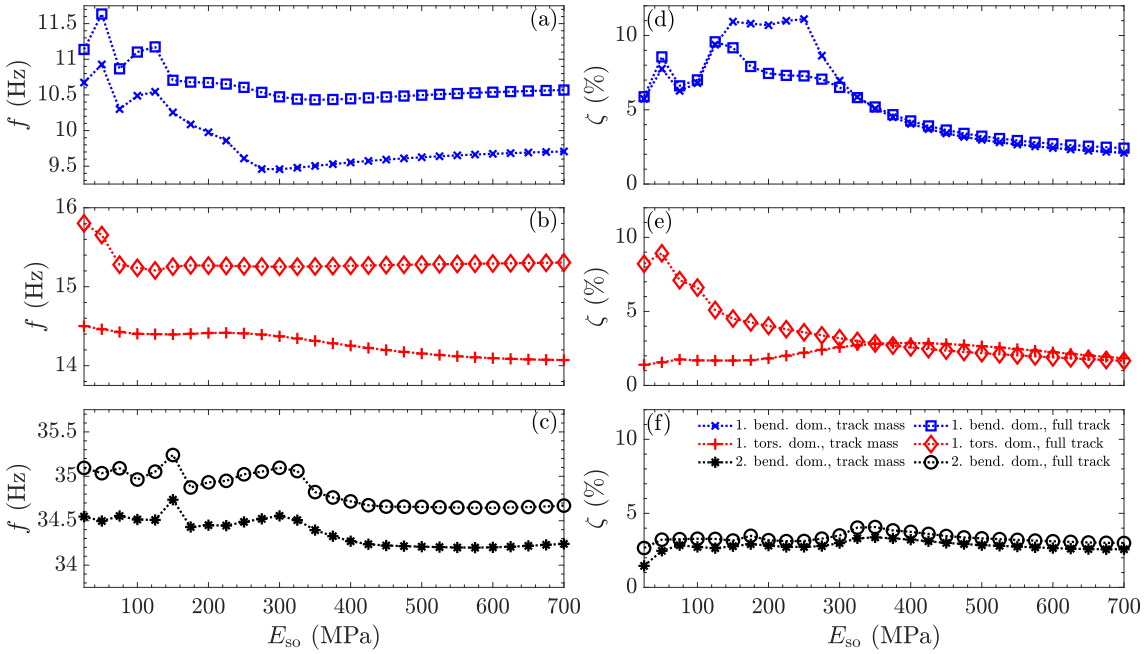



Fig. 20. Modal properties of the boundary element - finite element model as a function of soil modulus $E_{so}$. Model with full track vs. model with track mass. Natural frequency and effective modal damping ratio of (a),(d) first bending-dominated mode, (b),(e) first torsion-dominated mode, and (c),(f) second bending-dominated mode.

soil stiffness are not as pronounced for the second bending-dominated mode, where a larger modal damping ratio is computed for the model with full track over the entire range of soil stiffness considered.

The presented results clearly emphasize the importance of the modeling of the track when considering soil-structure interaction, since ignoring the track could lead to an overestimation of the modal damping ratios and, consequently, to a non-conservative design, or to an underestimation of the modal damping and to an overly conservative design of the structure. In addition, the influence of the track stiffness on the natural frequencies leads to a change in the response at resonance, where the vibrations are amplified.

## 4. Bridge response prediction due to moving train

As shown in the previous section, the consideration of the full track is of great importance for an accurate estimation of natural frequencies and modal damping ratios. Moreover, the material damping of the soil has a negligible influence on the properties of the bending-dominated and torsion-dominated structural modes. Therefore, the complete model considering track, bridge, foundations, and elastic soil, as illustrated in Fig. 6(a) ("Model 4" in Fig. 8), is considered for the response

estimation due to the passage of an ICE3 train model. The conventional train consisting of eight vehicles has the same vehicle length and axle spacing for all vehicles, as shown in Fig. 21. Due to the negligible variation in the weight of each vehicle,[49] all vertical axle loads, 32 in total, are considered uniformly with 166.03 kN, as shown in Fig. 21.

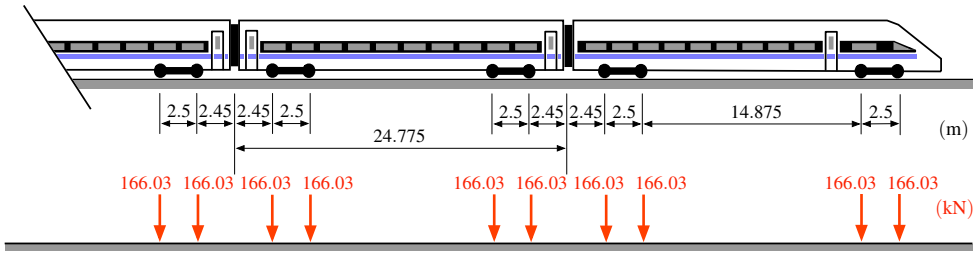



Fig. 21. Single force model of the ICE3 train.

In the numerical model, these moving concentrated loads are applied as time-dependent nodal loads at each node of the two rails. Since quadratic beam elements (B32) are used for the rails, the distribution of the moving load belonging to the $a$-th wheel $F^a = 166.03/2$ kN depends on the quadratic shape functions of an element $(e)$ evaluated at the load position $\zeta_a^{(e)}$ in the intrinsic element coordinate system at time $t$. The corresponding shape functions of node "1" located at the intrinsic coordinate position $\zeta_a^{(e)} = -1$, denoted by $N_1$, node "2", located at $\zeta_a^{(e)} = 1$, and the center node "3", located at $\zeta_a^{(e)} = 1$, read as[19]

$$N_1(\zeta_a^{(e)}(t)) = 0.5\left(-\zeta_a^{(e)}(t) + \left(\zeta_a^{(e)}(t)\right)^2\right) \quad , \quad N_2(\zeta_a^{(e)}(t)) = 0.5\left(\zeta_a^{(e)}(t) + \left(\zeta_a^{(e)}(t)\right)^2\right)$$
$$N_3(\zeta_a^{(e)}(t)) = 1 - \left(\zeta_a^{(e)}(t)\right)^2 \quad , \quad -1 \le \zeta_a^{(e)} \le 1 \tag{4.1}$$

Figure 22 shows an example of applying a nodal force at node $i$, which connects two elements $(e-1)$ and $(e)$, as well as the center node $i+1$ of element $(e)$. Subfigure 22(a) illustrates the time instance $t = t_i$, when the concentrated load $F^{(a)}$ is positioned at node $i$. Subfigure 22(b) shows the time-instance $t = t_{i+1}$, when the load is located at node $i+1$. Subfigure 22(c) shows the time-dependent loading $F_i^{(a)}(t)$, which is applied to node $i$ and resulting from the evaluation of $N_1$ and $N_2$. Subfigure 22(d) shows the load $F_{i+1}^{(a)}(t)$, which is applied to node $i+1$.

The response computation is performed using the transient time-domain formulations of Eqs (2.4) and (2.16), where a time step ratio of $\Delta t_{\mathrm{FE}}/\Delta t_{\mathrm{BE}} = 0.25$ is used between the boundary element and the finite element domains. Moreover, the time step of the boundary element domain is set to $\Delta t_{\mathrm{BE}} = \beta_{\mathrm{p}} L_{\mathrm{e}}/c_{\mathrm{p}}$, where the characteristic boundary element length is taken as $L_{\mathrm{e}} = 0.6$ m, corresponding to the

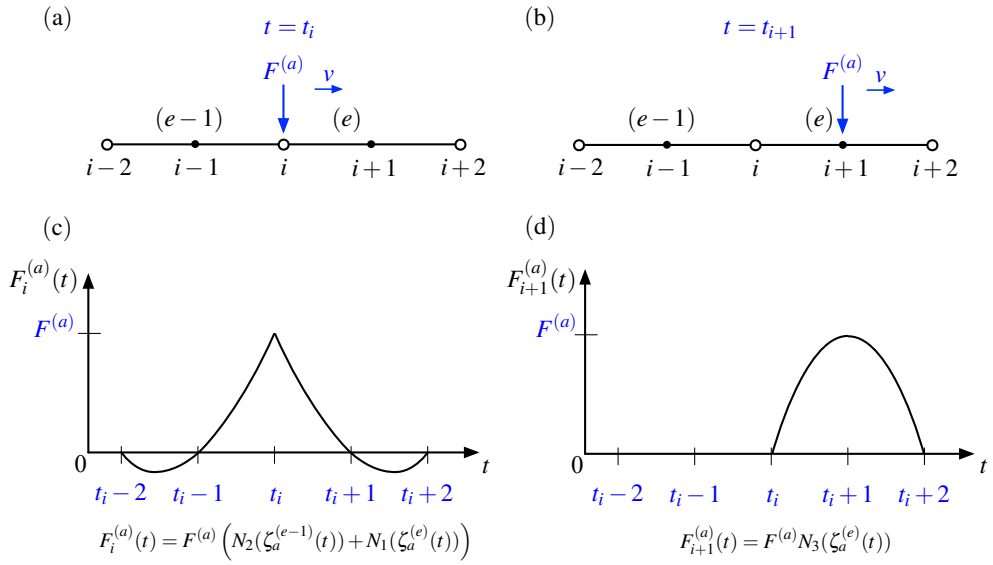



Fig. 22. Nodal loading due to $a$-th axle load $F^{(a)}$ moving over elements (e-1) and (e) at speed $v$. (a) Axle load at time $t_i$ located at node $i$. (b) Axle load at time $t_{(i+1)}$ located at node $i+1$. (c) Time-dependent load $F_i^{(a)}$ applied to the $i$-th node connecting elements $e-1$ and $e$ and (d) time-dependent load $F_{i+1}^{(a)}$ applied to the center node $i+1$.

shortest element dimension at the coupling interface, and the stability parameter is set to $\beta_{\mathrm{p}} = 0.5$. The coupling parameters of Table 1 are used for the iterative coupling of the finite and boundary element domains. Element integration is performed using the element subdivision scheme shown in Figs 1 and 2, with $N^{\mathrm{sub}} = 12$ subdivisions per intrinsic coordinate and $G^{\mathrm{sub}} = 2$ *Gauss* points per subdivision and coordinate direction. The density $\rho_{\mathrm{so}}$ and the *Poisson*'s ratio $\nu_{\mathrm{so}}$ are again taken from Table 2 and five different *Young*'s moduli in the range from $E_{\mathrm{so}} = 50$ MPa to $E_{\mathrm{so}} = 600$ MPa as well as one rigidly supported case ($E_{\mathrm{so}} = \infty$) are considered. The spatial and time discretization used allows an accurate representation of the structural response for frequencies below $100Hz$ in all cases considered. Therefore, the results are filtered using a low-pass *Butterworth* filter with a cut-off frequency of 100 Hz.

The computational results using these parameter configurations are summarized in Fig. 24 for train speeds in the range of $v = 30$ to $v = 120$ m/s. The results are shown separately for the paths P1, P2, and P3, which are located at the bridge deck, as shown in Fig. 6. Figures 24(a) to (c) depict the maximum absolute vertical bridge displacement $\max|w_{\mathrm{b}}|$ at the nodes of (a) path P1, (b) P2, (c) P3 and Figs 24(d) to (f) show the maximum absolute vertical bridge acceleration $\max|\ddot{w}_{\mathrm{b}}|$ at (d) P1, (e) P2, (f) P3. For the rigidly supported bridge ($E_{\mathrm{so}} = \infty$) and soils of higher stiffness ($E_{\mathrm{so}} = 400$ MPa and $E_{\mathrm{so}} = 600$ MPa), pronounced response peaks can be seen at

Table 7. Resonance speeds corresponding to the first bending–dominated mode $k = 1$ and $i = 3$ evaluated for the analyzed soil stiffnesses.

| $E_{\mathrm{so}}$ (MPa) | 50 | 100 | 200 | 400 | 600 | $\infty$ |
|---|---|---|---|---|---|---|
| $v_1^{(3)}$ (m/s) | 96.09 | 91.68 | 88.14 | 86.26 | 87.03 | 89.19 |

the so-called resonance speeds for repetitive loading defined by[50]

$$v_k^{(i)} = \frac{f_k d_{\mathrm{c}}}{i}$$

where $d_{\mathrm{c}}$ is the characteristic length of the train vehicles given by $d_{\mathrm{c}} = 24.775$ m (see Fig. 21) and $i = 1, 2, \ldots$. The peak responses in the considered train speed range are observed for the first bending-dominated mode $k = 1$ and $i = 3$ with the values for the resonance speeds listed in Table 7.

It is important to note that the resonance speeds listed in Table 7 contradict the notion, often found in literature,[4,6] that resonance speeds (and natural frequencies) must decrease with decreasing soil stiffness. While this trend may be valid for moderate to high soil stiffness, it is not valid for low soil stiffness, as can be seen in the natural frequency of the first bending-dominated mode depicted in Figs 14(a) and 19(a). Here, the natural frequency increases with very low soil stiffness. However, this observation is explained by the fact that the natural frequencies of a completely unsupported structure (i.e., $E_{\mathrm{so}} = 0$) are not necessarily lower than those of the same structure with supports (i.e., $E_{\mathrm{so}} = \infty$). Figure 23 shows this for a simple *Euler-Bernoulli* beam with length $L$, mass per unit length $\rho A$, and bending stiffness $EI$. As shown in Fig. 23(b), the bending frequency of the unsupported beam is more than twice that of the simply-supported beam (Fig. 23(a)). Based on these considerations, the increased natural frequencies and resonance speeds for soils with lower stiffness, as listed in Table 7, are justified.

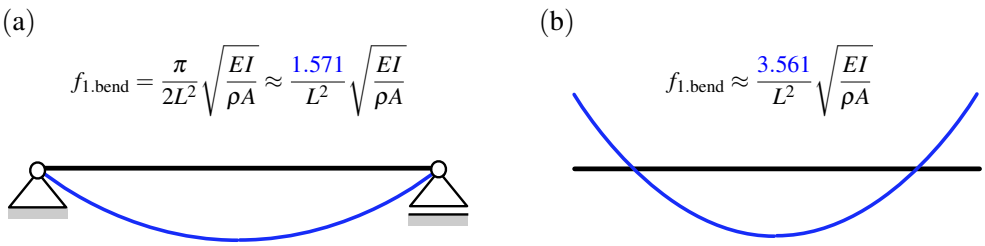



Fig. 23. First bending mode and natural frequency of an *Euler-Bernoulli* beam with (a) fixed supports and (b) free ends.

As the *Young*'s modulus decreases, the response peaks at resonance become significantly smaller for both $\max|w_{\mathrm{b}}|$ and $\max|\ddot{w}_{\mathrm{b}}|$. In addition, the maximum displacements for cases with lower soil stiffness increase over the entire train speed range and for non-resonant speeds. This increase in total vertical displacements

is most pronounced for the case with $E_{so} = 50$ MPa, where the displacements at the foundation and consequently the whole bridge are the largest due to the low support stiffness in the vertical direction. Although these results for computations with $E_{so} = 50$ MPa are theoretical, as this low stiffness would likely necessitate a piled foundation rather than the assumed spread footing, they may still serve as a valuable reference for more simplified soil-structure interaction models.

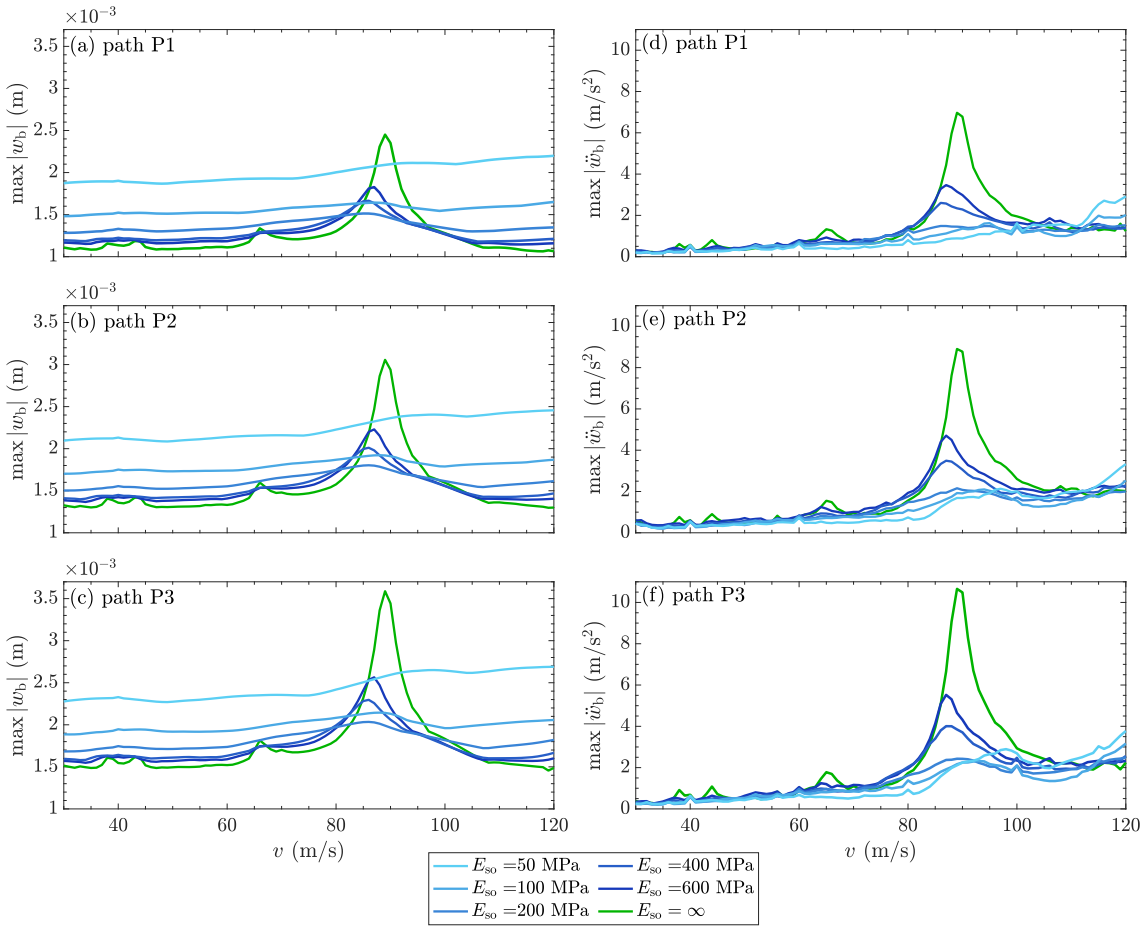



Fig. 24. Peak response of the maximum absolute vertical bridge deck displacement and the maximum absolute vertical bridge deck acceleration, evaluated at the path P1 ((a) and (d)), the path P2 ((b) and (e)), and the path P3 ((c) and (f)).

As can be seen by comparing the results for each path, the overall lowest response amplitudes are computed at the path P1, located at the main outer steel girder, and the highest at the opposite side of the cross-section at path P3. However, the results at P2 more closely reflect the mean deck response, with the peak

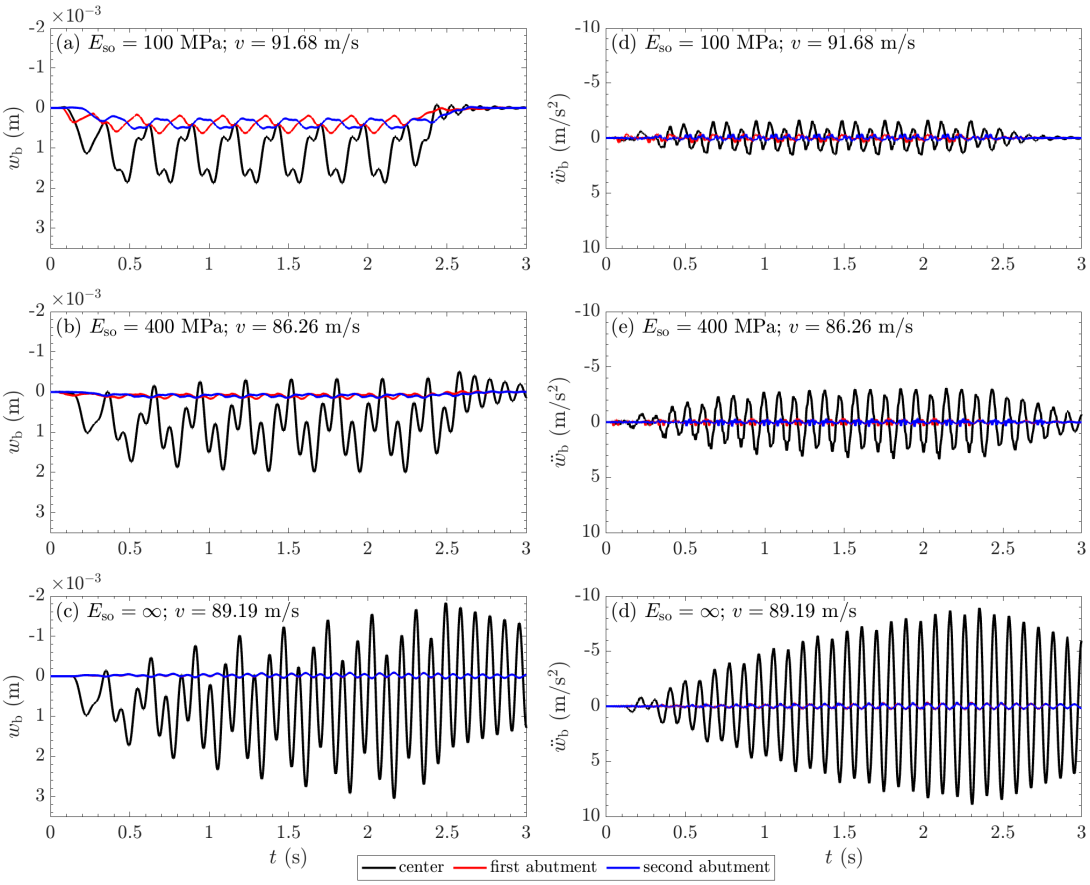



Fig. 25. Time histories computed for the vertical response of three points of path P2 located at the "first abutment", "second abutment", and "center" of the steel-girder bridge. Vertical displacements $w_b$ computed for (a) $E_{so} = 100$ MPa; $v = 91.68$ m/s, (b) $E_{so} = 400$ MPa; $v = 86.26$ m/s, (c) $E_{so} = \infty$; $v = 89.19$ m/s. Vertical accelerations $\ddot{w}_b$ computed for (d) $E_{so} = 100$ MPa; $v = 91.68$ m/s, (e) $E_{so} = 400$ MPa; $v = 86.26$ m/s, (f) $E_{so} = \infty$; $v = 89.19$ m/s.

acceleration $\max|\ddot{w}_b| = 8.90$ m/s$^2$ evaluated for the rigidly supported case at the resonance speed $v = 89.19$ m/s$^2$. The corresponding peak acceleration at resonance evaluated at P1 is $\max|\ddot{w}_b| = 6.97$ m/s$^2$ and $\max|\ddot{w}_b| = 10.66$ m/s$^2$ at P3. Therefore, it can be concluded that the maximum acceleration of the bridge deck varies by $+23.3$ % and $-21.5$ % with reference to that evaluated at the center path P2. This variance in the bridge response is a direct result of the asymmetry of the cross-section and, consequently, of the first bending-dominated mode. Since the location of the response peak is exactly at the nodes located at the midspan of the bridge, the relative variation of the response amplitudes at resonance by $+23.3$ % and $-21.5$ % matches that of the amplitudes of the corresponding mode shape of the first bending-dominated mode at the same node positions.

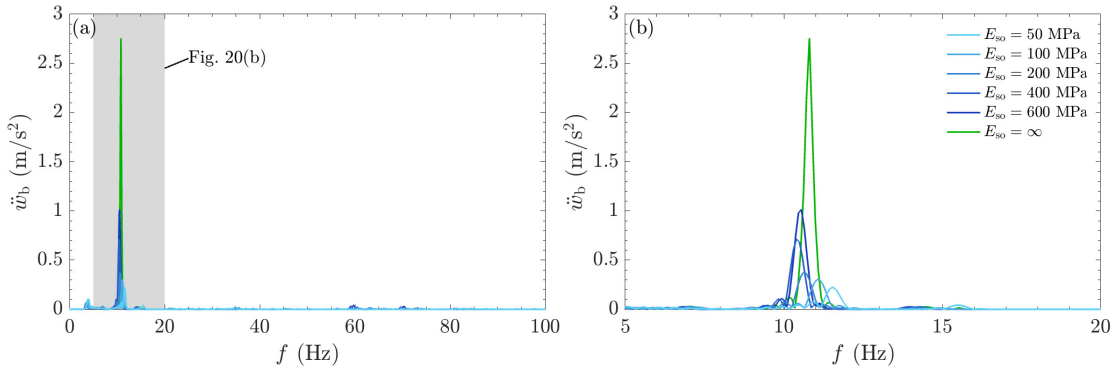



Fig. 26. Envelope of the bridge deck accelerations in frequency domain evaluated at the resonance speeds for different soil *Young*'s moduli for (a) $0 \leq f \leq 100$ Hz and (b) $5 \leq f \leq 20$ Hz.

Figure 25 displays the time histories evaluated at three separate points along the central path P2 for the excitation due to the ICE3 train moving at resonance speeds. To assess the impact of soil stiffness on the displacements and accelerations at the foundation locations, results from the point at the "first abutment" and at the "second abutment" are compared to the "center" point on the midpoint of the bridge deck for various soil stiffness levels. Figures 25(a), (b), and (c) show the displacement responses assuming $E_{so} = 100$ MPa, $E_{so} = 400$ MPa, and $E_{so} = \infty$ respectively. Figures 25(d), (e), and (f) show the corresponding acceleration responses. For the computations in Fig. 25, the resonance speeds corresponding to the values in Table 7 were applied as train speeds. As can be seen by comparing displacement responses evaluated at different soil stiffnesses (Figs 25(a), (b), and (c)), very soft soil ($E_{so} = 100$ MPa) leads to significant displacements at the abutments. Increasing the soil stiffness yields lower displacements at the abutments and higher displacements at the center of the bridge. Similarly, increased maximum accelerations at the bridge center are observed with increased soil stiffness (cf. Figs 25(d), (e), and (f)). Overall, there is lower damping for stiffer soil ($E_{so} = 400$ MPa) or rigid soil ($E_{so} = \infty$).

Figure 26 shows the envelope over all nodal results of the vertical bridge deck accelerations at P1, P2, and P3 transformed into the frequency domain and evaluated for train passages at the resonance speeds corresponding to the different soil stiffnesses. Here, Fig. 26(a) shows the frequency content over the total frequency range considered. It is clearly visible that the largest acceleration peaks occur at the frequencies corresponding to the natural frequencies of the first bending-dominated mode close to 10.80 Hz, and significantly smaller peaks can be observed close to the natural frequencies of the second bending-dominated mode around 34.87 Hz. No significant acceleration response is observed at frequencies higher than that of the second bending-dominated mode. In Fig. 26(b) only the frequency content close to the natural frequencies of the first bending-dominated mode is shown. As can be

seen, the response peaks computed for soil *Young*'s of $E_{\mathrm{so}} = 200$ MPa, $E_{\mathrm{so}} = 400$ MPa, and $E_{\mathrm{so}} = 600$ MPa occurs at lower frequencies than for the rigidly supported bridge and at higher frequencies for $E_{\mathrm{so}} = 50$ MPa and $E_{\mathrm{so}} = 100$ MPa. This observation further confirms the soil stiffness dependent shift of the natural frequency to higher or lower frequencies. The significant reduction of the acceleration response at resonance due to the increased damping from soil-structure interaction is also visible in Fig. 26.

## 5. Conclusions

This paper presents a comprehensive three-dimensional numerical study examining the dynamic response of a steel-girder railway bridge, accounting for soil-structure interaction. A coupled finite element-boundary element modeling approach was employed to model the interaction between the bridge, track, foundations, and supporting soil. This formulation was applied in the frequency and time domains to analyze how soil stiffness and track modeling impact modal properties and the transient response caused by moving train loads. Based on the results, the following conclusions can be drawn:

- The three-dimensional coupled finite element-boundary element model allows for a combined frequency- and time-domain assessment of soil-structure interaction effects in steel railway bridges. This model provides consistent predictions of modal properties and transient response under train loading.
- Explicit modeling of the track and supporting soil can significantly alter the dynamic behavior of steel railway bridges. This affects both stiffness and damping, showing that simplified modeling approaches may lead to inaccurate response predictions.
- Soil-structure interaction causes shifts in the natural frequencies of the primary structural modes.The direction and magnitude of these shifts depend on soil stiffness and they directly influence resonance conditions.
- In addition to the primary and secondary structural modes governed by bridge deformations, non-structural modes dominated by soil deformation were identified. While modal phase collinearity allows for a clear distinction between these modes when natural frequencies are well separated, it becomes less reliable for closely spaced frequencies, where similar damping ratios and mode shapes may occur.
- Soil-structure interaction primarily increases effective modal damping through geometric damping associated with wave propagation in the supporting soil. For the first bending-dominated mode, damping ratios were observed that were nearly an order of magnitude higher than current design recommendations, primarily due to geometric damping associated with wave propagation in the soil. The largest damping ratio of $\zeta = 9.58$ % was

observed for the first bending-dominated mode of the soil-structure model with full track in soil with low stiffness and a *Young*'s modulus of $E_{\mathrm{so}} = 125$ MPa. The modal damping ratio of the first bending-dominated mode gradually decreases with increasing soil stiffness. However, even for the soil with a *Young*'s modulus of $E_{\mathrm{so}} = 700$ MPa, the largest considered value, the damping ratio of $\zeta = 2.42$ % exceeds the reference value of $\zeta = 1.01$ %, computed for the model without soil-structure interaction.

- Time-domain analyses demonstrate that the increased effective damping significantly reduces bridge deck accelerations at resonance speeds. For the structural model with a full track and no consideration of soil-structure interaction, the maximum deck acceleration response due to excitation from an ICE3 single-force model was 10.66 m/s$^2$. Including soil-structure interaction in the coupled finite element - boundary element model reduced the maximum deck acceleration to 5.5 m/s$^2$ for a soil *Young*'s modulus of $E_{\mathrm{so}} = 600$ MPa, 4.0 m/s$^2$ for $E_{\mathrm{so}} = 400$ MPa, and less than 3.5 m/s$^2$ for soils with lower stiffness. This highlights the importance of accounting for soil-structure interaction when assessing the dynamics of steel railway bridges to avoid overly conservative results.

The present study is based on a homogeneous elastic representation of the soil and idealized bearing conditions. Therefore, the presented results do not cover inhomogeneous soil conditions, such as those found in layered soils with significant differences in soil types, or soil layers on top of very stiff bedrock. Future studies should investigate the influence of stratified soil profiles, nonlinear track behavior, and bearings with reduced stiffness, which could lead to a partial dynamic decoupling between the bridge and the foundation. Although more computationally efficient frequency- and time-domain formulations may be adopted for future applications, the physical trends and conclusions reported in this study are valid regardless of the specific numerical implementation. Additionally, extending the time-domain formulation to include fully coupled train-bridge interaction models would further enhance the applicability of the approach for realistic serviceability assessments.

The coupled finite element-boundary element approach presented here provides a suitable reference model for analyzing soil-structure interaction in railway bridges. The results can support the calibration of simplified, design-oriented beam models and inform more realistic serviceability evaluations under train loading. Additionally, the time-domain formulation can be extended to include fully coupled train-bridge interaction analyses.

## Acknowledgements

The computational results presented have been achieved (in part) using the HPC infrastructure LEO of the Universität Innsbruck.

## ORCID

Paul König - https://orcid.org/0000-0002-3820-9200
Christoph Adam - https://orcid.org/0000-0001-9408-6439


## Appendix A. Model Parameters

Table 8. Parameters of the steel-girder bridge.[37]

| Description | Variable | Unit | Value |
|---|---|---|---|
| Main girder web | $h_1$, $t_{\mathrm{web1}}$ | mm | 2090, 20 |
| Main girder flange | $h_{\mathrm{f1}}^{\mathrm{u}}$, $t_{\mathrm{f1}}^{\mathrm{u}}$, $h_{\mathrm{f1}}^{\mathrm{l}}$, $t_{\mathrm{f1}}^{\mathrm{l}}$ | mm | 200, 60, 310, 60 |
| Secondary T-girder | $h_2$, $t_{\mathrm{web2}}$, $h_{\mathrm{f2}}$, $t_{\mathrm{f2}}$ | mm | 1140, 12, 350, 60 |
| Through girder | $h_3$, $t_{\mathrm{web3}}$, $h_{\mathrm{f3}}$, $t_{\mathrm{f3}}$ | mm | 1100, 20, 747, 80 |
| Transversal girder | $h_4$, $t_{\mathrm{web4}}$, $h_{\mathrm{f4}}$, $t_{\mathrm{f4}}$ | mm | 1100, 20, 350, 30 |
| Deck plate | $t_{\mathrm{deck}}$ | mm | 35 |
| Steel material | $E_{\mathrm{st}}$, $\rho_{\mathrm{st}}$, $\nu_{\mathrm{st}}$ | GPa, kg/m$^3$, - | 210, 7850, 0.3 |

Table 9. Parameters of the ballast in the finite element model.[11,39]

| Description | Variable | Unit | Value |
|---|---|---|---|
| Ballast dimensions | $h_{\mathrm{b}}$, $b_{\mathrm{ballast}}^{\mathrm{l}}$, $b_{\mathrm{ballast}}^{\mathrm{u}}$ | mm | 700, 2335, 1500 |
| Ballast material | $E_{\mathrm{b}}$, $\rho_{\mathrm{b}}$, $\nu_{\mathrm{b}}$ | MPa, kg/m$^3$, - | 120, 1500, 0.2 |

Table 10. Parameters of the foundation.

| Description | Variable | Unit | Value |
|---|---|---|---|
| Mass | $\tilde{m}_1$ | kg | 230338 |
| Base area | $A_0$ | m$^2$ | 34.4 |
| Reinf. concrete material | $E_{\mathrm{cr}}$, $\rho_{\mathrm{cr}}$, $\nu_{\mathrm{cr}}$ | GPa, kg/m$^3$, - | 32.837, 2500, 0.2 |

Table 11. Parameters of the rail and sleeper in the finite element model.[51,52]

| Description | Variable | Unit | Value |
|---|---|---|---|
| Half gauge distance | $b$ | mm | 720 |
| Rail profile (UIC 60) | $A_{\mathrm{r}}$, $I_{\mathrm{y}}$, $I_{\mathrm{z}}$ | cm$^2$, cm$^4$, cm$^4$, | 76.70, 3038.30, 512.30 |
| Sleeper spacing | $e$ | mm | 600 |
| Sleeper dimensions | $b_{\mathrm{sl}}$, $h_{\mathrm{sl}}$, $l_{\mathrm{sl}}$ | mm | 230, 200, 2600 |
| Sleeper material | $E_{\mathrm{sl}}$, $\rho_{\mathrm{sl}}$, $\nu_{\mathrm{sl}}$ | GPa, kg/m$^3$, - | 32.837, 2400, 0.2 |
| Rail pad stiffness | $k_{\mathrm{rx}}$, $k_{\mathrm{ry}}$, $k_{\mathrm{rz}}$ | MN/m | 49, 100, 150 |

## References


1. European Rail Research Institute (ERRI) D-214 Committee, Rail bridges for speeds over 200 km/h. RP 9, Final report, tech. rep., European Rail Research Institute (1999).
2. EN1990-A1, Eurocode 0: Basis of structural design. Amendment A1: Application for Bridges (2013).
3. M. Ülker-Kaustell, R. Karoumi and C. Pacoste, Simplified analysis of the dynamic soil–structure interaction of a portal frame railway bridge, *Engineering Structures* **32** (2010) 3692–3698.
4. A. Romero, M. Solís, J. Domínguez and P. Galvín, Soil–structure interaction in resonant railway bridges, *Soil Dynamics and Earthquake Engineering* **47** (2013) 108–116.
5. C. Svedholm, C. Pacoste and R. Karoumi, Modal properties of simply supported railway bridges due to soil-structure interaction, in *Proceedings of the 5th International Conference on Computational Methods in Structural Dynamics and Earthquake Engineering* eds. M. Papadrakakis, V. Papadopoulos and V. Plevris COMPDYN, (Crete, Greece, 2015), pp. 1709–1719.
6. A. Doménech, M. Martínez-Rodrigo, A. Romero and P. Galvín, On the basic phenomenon of soil-structure interaction on the free vibration response of beams: Application to railway bridges, *Engineering Structures* **125** (2016) 254–265.
7. P. Galvín, A. Romero, E. Moliner, D. P. Connolly and M. D. Martínez-Rodrigo, Fast simulation of railway bridge dynamics accounting for soil–structure interaction, *Bulletin of Earthquake Engineering* **20**(7) (2022) 3195–3213.
8. P. König, P. Salcher, C. Adam and B. Hirzinger, Dynamic analysis of railway bridges exposed to high-speed trains considering the vehicle–track–bridge–soil interaction, *Acta Mechanica* **232**(11) (2021) 4583–4608.
9. P. König, P. Salcher and C. Adam, An efficient model for the dynamic vehicle-track-bridge-soil interaction system, *Engineering Structures* **253** (2022) p. 113769.
10. J. Chordà-Monsonís, J. Sánchez-Quesada, E. Moliner, A. Romero, P. Galvín and M. Martínez-Rodrigo, Efficient simulation of the soil–structure interaction on the dynamic response of a portal frame railway bridge, *Structures* **82** (2025) p. 110600.
11. A. Zangeneh, C. Svedholm, A. Andersson, C. Pacoste and R. Karoumi, Identification of soil-structure interaction effect in a portal frame railway bridge through full-scale dynamic testing, *Engineering Structures* **159** (2018) 299–309.
12. EN1991-2, Eurocode 1: Actions on structures - Part 2: traffic loads on bridges (consolidated version) (2012).
13. P. Montenegro, E. Laligant, F. Pimenta, A. Silva, O. Ahmed, C. Laurent and A. Andersson, Towards improved normative definitions of damping in railway bridges: Insights from the inbridge4eu european experimental database, *Engineering Structures* **359** (2026) p. 122666.
14. A. Stollwitzer, L. Bettinelli and J. Fink, The longitudinal track-bridge interaction of ballasted track in railway bridges: Experimental determination of dynamic stiffness and damping characteristics, *Engineering Structures* **274** (2023) p. 115115.
15. P. König and C. Adam, A model considering the longitudinal track–bridge interaction in ballasted railway bridges subjected to high-speed trains, *Acta Mechanica* **235**(3) (2024) 1395–1418.
16. P. Salcher and C. Adam, Estimating exceedance probabilities of railway bridge vibrations in the presence of random rail irregularities, *International Journal of Structural Stability and Dynamics* **20** (2020) p. 2041005.
17. R. Allahvirdizadeh, A. Andersson and R. Karoumi, Probabilistic dynamic design curves optimized for high-speed reinforced concrete railway bridges using first-order

reliability method, *International Journal of Structural Stability and Dynamics* **25**(24) (2025) p. 2540012.
18. R. Allahvirdizadeh, E. Moliner and P. Museros, Data-driven relationship for reduction factor of ballasted railway bridge deflections due to load distribution within track, *International Journal of Structural Stability and Dynamics* **25**(24) (2025) p. 2540017.
19. Abaqus, *ABAQUS/Standard User's Manual, Version 2016* (Dassault Systèmes, 2015).
20. W. Chew and Q. Liu, Perfectly matched layers for elastodynamics: A new absorbing boundary condition, *Journal of Computational Acoustics* **04** (1997).
21. N. Zhang, H. Xia, W. W. Guo and G. De Roeck, A vehicle-bridge linear interaction model and its validation, *International Journal of Structural Stability and Dynamics* **10**(02) (2010) 335–361.
22. J. Domínguez, *Boundary Elements in Dynamics* (Computational Mechanics Publications, Southampton, United Kingdom, 1993).
23. K. Bathe, *Finite element procedures* (Bathe, Boston, Mass., 2006).
24. M. Marrero and J. Domínguez, Numerical behavior of time domain bem for three-dimensional transient elastodynamic problems, *Engineering Analysis with Boundary Elements* **27**(1) (2003) 39–48.
25. W. Mansur, *A Time-Stepping Technique to Solve Wave Propagation Problems using the Boundary Element Method* (Universität of Southampton, Southampton, England, 1983).
26. V. Mantič, A new formula for the C-matrix in the Somigliana identity, *Journal of Elasticity* **33**(3) (1993) 191–201.
27. P. König, *Substructure approaches for the analysis of track-bridge-soil systems subjected to high-speed trains* (Universität Innsbruck, Innsbruck, Austria, 2024).
28. M. Guiggiani and A. Gigante, A General Algorithm for Multidimensional Cauchy Principal Value Integrals in the Boundary Element Method, *Journal of Applied Mechanics* **57**(4) (1990) 906–915.
29. M. Guiggiani, Computing principal-value integrals in 3-d bem for time-harmonic elastodynamics – a direct approach, *Communications in Applied Numerical Methods* **8**(3) (1992) 141–149.
30. G. Yu, W. Mansur, J. Carrer and S. Lie, A more stable scheme for bem/fem coupling applied to two-dimensional elastodynamics, *Computers & Structures* **79**(8) (2001) 811–823.
31. A. K. Chopra, *Dynamics of Structures: Theory and Applications to Earthquake Engineering*, 5 edn. (Pearson, 2017).
32. O. C. Zienkiewicz, R. L. Taylor and J. Z. Zhu, *The Finite Element Method: Its Basis and Fundamentals*, 7 edn. (Butterworth-Heinemann, Oxford, 2013).
33. O. C. Zienkiewicz, D. W. Kelly and P. Bettess, The coupling of the finite element method and boundary solution procedures, *International Journal for Numerical Methods in Engineering* **11**(2) (1977) 355–375.
34. F. Araújo, W. Mansur and L. Nishikava, Determination of 3D time domain responses in layered media by using a coupled BE/FE process, *WIT Transactions on Modelling and Simulation* **21** (1998) 587–596.
35. O. von Estorff and C. Hagen, Iterative coupling of fem and bem in 3d transient elastodynamics, *Engineering Analysis with Boundary Elements* **30**(7) (2006) 611–622.
36. J. P. Wolf and A. Deeks, *Foundation Vibration Analysis: A Strength of Materials Approach* (Butterworth-Heinemann, Oxford, 2004).
37. P. Salcher and C. Adam, Modeling of dynamic train–bridge interaction in high–speed railways, *Acta Mechanica* **226**(8) (2015) 2473–2495.
38. B. Biondi, G. Muscolino and A. Sofi, A substructure approach for the dynamic analysis

of train–track–bridge system, *Computers & Structures* **83**(28-30) (2005) 2271–2281.
39. A. Zangeneh, *Dynamic Soil-Structure Interaction Analysis of High-Speed Railway Bridges: Efficient Modeling Techniques and Experimental Testing* (KTH Royal Institute of Technology, Stockholm, Schweden, 2021).
40. American Society of Civil Engineers, Minimum design loads and associated criteria for buildings and other structures (2022).
41. R. W. Clough and J. Penzien, *Dynamics of Structures* (McGraw-Hill, New York, 1993).
42. R. R. Craig and A. J. Kurdila, *Fundamentals of Structural Dynamics*, 2 edn. (John Wiley & Sons, 2006).
43. A. Stollwitzer, L. Bettinelli and J. Fink, Vertical track–bridge interaction in railway bridges with ballast superstructure: Experimental analysis of dynamic stiffness and damping behavior, *International Journal of Structural Stability and Dynamics* **25**(24) (2025) p. 2540008.
44. H. Van der Auweraer, P. Guillaume, P. Verboven and S. Vanlanduit, Application of a fast-stabilizing frequency domain parameter estimation method, *Journal of Dynamic Systems, Measurement, and Control* **123**(4) (2001) 651–658.
45. B. Peeters, H. Van der Auweraer, P. Guillaume and J. Leuridan, The polymax frequency-domain method: A new standard for modal parameter estimation? shock and vibration, *Special Issue Dedicated to Professor Bruno Piombo* **395** (01 2004) p. 523692.
46. A. Zangeneh, S. François, G. Lombaert and C. Pacoste, Modal analysis of coupled soil-structure systems, *Soil Dynamics and Earthquake Engineering* **144** (2021) p. 106645.
47. R. S. Pappa, K. B. Elliott and A. Schenk, Consistent-mode indicator for the eigensystem realization algorithm, *Journal of Guidance, Control, and Dynamics* **16**(5) (1993) 852–858.
48. M. Vigsø, T. Kabel, M. Tarpø, R. Brincker and C. Georgakis, Operational modal analysis and fluid-structure interaction, in *Proc. of the International Conference on Noise and Vibration Engineering 2018 (ISMA2018)* ISMA, (Leuven, Belgium, 2018).
49. G. K. Nguyen, J. M. Goicolea and F. Galbadón, Comparison of dynamic effects of high-speed traffic load on ballasted track using a simplified two-dimensional and full three-dimensional model, *Proceedings of the Institution of Mechanical Engineers, Part F: Journal of Rail and Rapid Transit* **228**(2) (2012) 128–142.
50. Y. B. Yang, J. D. Yau and Y. S. Wu, *Vehicle–Bridge Interaction Dynamics* (World Scientific, 2004).
51. S. L. Grassie, R. W. Gregory, D. Harrison and K. L. Johnson, The dynamic response of railway track to high frequency vertical excitation, *Journal of Mechanical Engineering Science* **24**(2) (1982) 77–90.
52. S. L. Grassie, A contribution to dynamic design of railway track, *Vehicle System Dynamics* **20** (1992) 195–209.